

# Electron Transport in Wide Energy Gap Semiconductors

by

Reddiprasad Cheekoori

A THESIS SUBMITTED IN PARTIAL FULFILLMENT OF  
THE REQUIREMENTS FOR THE DEGREE OF

MASTER OF APPLIED SCIENCE

in

The College of Graduate Studies

(Electrical Engineering)

THE UNIVERSITY OF BRITISH COLUMBIA

(Okanagan)

January, 2012

© Reddiprasad Cheekoori 2012

# Abstract

The dependence of the low-field electron drift mobility on the crystal temperature is determined for a number of wide energy gap semiconductors of interest. The materials considered include gallium nitride, aluminium nitride, indium nitride, and zinc oxide; while indium nitride is not a wide energy gap semiconductor in of itself, alloys of indium nitride with gallium nitride are. For the bulk results, it is found that indium nitride exhibits the highest low-field electron drift mobility while aluminium nitride exhibits the lowest low-field electron drift mobility. This is related to the small effective mass of electrons in indium nitride and the large effective mass of electrons in aluminium nitride. For the case of electrons confined within a two-dimensional electron gas, it is found that the low-field electron drift mobility exceeds that corresponding to the bulk material. This is due to the enhanced screening that electron concentrations exceeding the bulk ionized impurity concentrations level offer, i.e., surplus electrons act to further screen the ionized impurities; in a two-dimensional electron gas, the electron concentrations may far exceed those found in a bulk material. Recommendations for further study are suggested.

# Table of Contents

<b>Abstract</b> . . . . .	ii
<b>Table of Contents</b> . . . . .	iii
<b>List of Tables</b> . . . . .	vi
<b>List of Figures</b> . . . . .	vii
<b>Acknowledgements</b> . . . . .	xx
<b>1 Introduction</b> . . . . .	1
<b>2 Material properties</b> . . . . .	10
2.1 Material properties and electron device performance . . . . .	10
2.2 The distribution of electronic states . . . . .	11
2.3 Direct and indirect energy gaps . . . . .	15
2.4 Temperature dependence of the energy gap . . . . .	15
2.5 Wide energy gap semiconductors . . . . .	17
2.6 Other material properties and their dependence on the energy gap . . . . .	19

*Table of Contents*

---

<b>3</b>	<b>Electron drift mobility in semiconductors</b>	27
3.1	Electron drift mobility and scattering mechanisms	27
3.2	The random thermal motion of charge carriers in the absence of an applied electric field	28
3.3	Electron transport under the action of an applied electric field	29
3.4	Scattering mechanisms	33
3.5	Analytical expressions for the contributions to the low-field electron drift mobility	36
3.5.1	Ionized impurity scattering	36
3.5.2	Polar optical phonon scattering	38
3.5.3	Piezoelectric scattering	38
3.5.4	Acoustic phonon deformation potential scattering	40
3.6	Electron transport in a two-dimensional electron gas	41
<b>4</b>	<b>Results</b>	44
4.1	Overview	44
4.2	Material parameter selections	45
4.3	GaN bulk results	47
4.4	AlN bulk results	55
4.5	InN bulk results	70
4.6	ZnO bulk results	79
4.7	A comparison of the bulk results	93
4.8	Two-dimensional electron gas	95
<b>5</b>	<b>Conclusions</b>	100

*Table of Contents*

---

**References** . . . . . 104

# List of Tables

4.1	The material parameters corresponding GaN, AlN, and InN. These parameter selections are from O'Leary <i>et al.</i> [15]. . . .	46
4.2	The material parameters corresponding to ZnO. The ZnO parameter selections are from Albrecht <i>et al.</i> [21]. . . . .	47

# List of Figures

- 1.1 The intrinsic electron concentrations, for c-Si, c-Ge, and c-GaAs, as a function of the reciprocal temperature. . . . . 3
- 1.2 The energy gap represents the difference in energy between top of the valence band and the bottom of the conduction band. At zero temperature, the valence band is fully occupied and the conduction band is completely unoccupied. . . . . 4
- 1.3 The room temperature energy gaps associated with a variety of compound semiconductors. The data depicted in this figure is from Adachi [8]. . . . . 6
- 1.4 The velocity-field characteristics associated with c-Si and c-GaAs. Logarithmic scales are employed for both axes. For both cases, the crystal temperature is set to 300 K. . . . . 8
  
- 2.1 The electron energy levels associated with an isolated C atom. This figure is after Streetman [3]. . . . . 12
- 2.2 The formation of the energy gap within C. This figure is after Streetman [3]. This particular image is from Malik [12]. . . . 14

*List of Figures*

---

2.3	A one-dimensional depiction of the energy band diagrams associated with c-Si and c-GaAs. This figure is after Streetman [3]. . . . .	16
2.4	The energy gaps associated with c-Si and c-GaAs as a function of the crystal temperature. These plots are determined using the Varshni relationship, i.e., Eq. (2.1), for the empirical parameter selections suggested in the text. . . . .	18
2.5	The differences in the energy gap between a semiconductor and a wide energy gap semiconductor . . . . .	20
2.6	The electron effective mass as a function of the energy gap for selected III-V and II-VI semiconductors. The direct energy gap materials are depicted with the solid points, while the indirect energy gap materials are represented with the open points. Most of the data depicted in this figure is from Adachi [8]. The InN data, however, is from O’Leary <i>et al.</i> [15].	21
2.7	The breakdown electric field as a function of the energy gap for selected III-V and II-VI semiconductors. The direct energy gap materials are depicted with the solid points, while the indirect energy gap materials are depicted with the open points. The data depicted in this figure is from Adachi [8]. . .	22

*List of Figures*

---

2.8	The static relative dielectric constant, $k_s = \epsilon_s/\epsilon_o$ , as a function of the energy gap for selected III-V and II-VI semiconductors. The direct energy gap materials are depicted with the solid points, while the indirect energy gap materials are depicted with the open points. The data depicted in this figure is from Adachi [8]. . . . .	24
2.9	The high-frequency relative dielectric constant, $k_\infty = \epsilon_\infty/\epsilon_o$ , as a function of the energy gap for selected III-V and II-VI semiconductors. The direct energy gap materials are depicted with the solid points, while the indirect energy gap materials are depicted with the open points. Most of the data depicted in this figure is from Adachi [8]. The InN data, however, is from O’Leary <i>et al.</i> [15]. . . . .	25
2.10	The electron affinity as a function of the energy gap for selected III-V and II-VI semiconductors. The direct energy gap materials are depicted with the solid points, while the indirect energy gap materials are depicted with the open points. The data depicted in this figure is from Adachi [8]. . . . .	26

*List of Figures*

---

3.1	The random thermal motion of a representative electron in a semiconductor crystal in the absence of an applied electric field. This particular electron engages in scattering a number of times, the numbers 2 through 12 representing the scattering events that occur; number 1 corresponds to this particular electron's initial position. Between scattering events, the electron propagates with no acceleration. The scattering events are seen to randomize the direction of the electron transit. This figure is after Streetman [3]. . . . .	30
3.2	The different scattering mechanisms that can occur in semiconductors. The particular scattering mechanisms that we examine for the purposes of this analysis are presented with the bold font. This figure is after Adachi [8]. . . . .	34
3.3	The energy band diagram associated with c-GaAs. A three-valley representation of this band diagram for the conduction band is depicted beneath a more exact one-dimensional representation of the energy band diagram corresponding to this material [16, 17]. . . . .	35
3.4	The energy band diagram of an AlGa <sub>N</sub> /Ga <sub>N</sub> high electron mobility transistor. A quantum well is formed in the Ga <sub>N</sub> layer close to the AlGa <sub>N</sub> /Ga <sub>N</sub> interface. Mobile electrons, contributed from the AlGa <sub>N</sub> and Ga <sub>N</sub> layers, are trapped in the quantum well that is present, thus forming a two-dimensional electron gas [20]. . . . .	42

*List of Figures*

---

4.1	The ionized impurity contribution to the low-field electron drift mobility as a function of the crystal temperature for the case GaN. For all cases, the electron concentration, $n$ , is set to the bulk ionized impurity concentration, $N_T$ . . . . .	48
4.2	The polar optical phonon contribution to the low-field electron drift mobility as a function of the crystal temperature for the case of GaN. . . . .	50
4.3	The piezoelectric contribution to the low-field electron drift mobility as a function of the crystal temperature for various selections of the electron concentration for the case of GaN. . . . .	51
4.4	The acoustic deformation potential contribution to the low-field electron drift mobility as a function of the crystal temperature for the case of GaN. . . . .	53
4.5	The polar optical phonon, piezoelectric, and acoustic deformation potential contributions to the low-field electron drift mobility, and the combined low-field electron drift mobility, plotted as functions of the crystal temperature for the case of GaN. For the purposes of this analysis, the ionized impurity contribution is neglected, i.e., it is set to infinity. The electron concentration, $n$ , is set to $10^{17}$ cm <sup>-3</sup> for all cases. . . . .	54

*List of Figures*

---

4.6	The combined low-field electron drift mobility as a function of the crystal temperature with the polar optical phonon, piezoelectric, and acoustic deformation potential scattering mechanisms taken into account for various electron concentrations for the case of GaN. For all cases, the ionized impurity contribution is neglected, i.e., it is set to infinity. . . . .	56
4.7	The ionized impurity, polar optical phonon, piezoelectric, and acoustic deformation potential contributions to the low-field electron drift mobility as a function of the crystal temperature for the case of GaN. The bulk ionized impurity concentration, $N_T$ , is set to $10^{17} \text{ cm}^{-3}$ . The electron concentration, $n$ , is set to the bulk ionized impurity concentration, $N_T$ . . . . .	57
4.8	The combined low-field electron drift mobility as a function of the crystal temperature for the case of GaN. The contributions to the low-field electron drift mobility considered include those related to the ionized impurity, polar optical phonon, piezoelectric, and acoustic deformation potential scattering mechanisms. For all cases, the electron concentration, $n$ , is set to the bulk ionized impurity concentration, $N_T$ . . . . .	58
4.9	The ionized impurity contribution to the low-field electron drift mobility as a function of the crystal temperature for the case AlN. For all cases, the electron concentration, $n$ , is set to the bulk ionized impurity concentration, $N_T$ . . . . .	60

*List of Figures*

---

4.10	The polar optical phonon contribution to the low-field electron drift mobility as a function of the crystal temperature for the case of AlN. . . . .	61
4.11	The piezoelectric contribution to the low-field electron drift mobility as a function of the crystal temperature for various selections of the electron concentration for the case of AlN. . . . .	62
4.12	The acoustic deformation potential contribution to the low-field electron drift mobility as a function of the crystal temperature for the case of AlN. . . . .	64
4.13	The polar optical phonon, piezoelectric, and acoustic deformation potential contributions to the low-field electron drift mobility, and the combined low-field electron drift mobility, plotted as functions of the crystal temperature for the case of AlN. For the purposes of this analysis, the ionized impurity contribution is neglected, i.e., it is set to infinity. The electron concentration, $n$ , is set to $10^{17} \text{ cm}^{-3}$ for all cases. . . . .	65
4.14	The combined low-field electron drift mobility as a function of the crystal temperature with the polar optical phonon, piezoelectric, and acoustic deformation potential scattering mechanisms taken into account for various electron concentrations for the case of AlN. For all cases, the ionized impurity contribution is neglected, i.e., it is set to infinity. . . . .	67

*List of Figures*

---

4.15	The ionized impurity, polar optical phonon, piezoelectric, and acoustic deformation potential contributions to the low-field electron drift mobility as a function of the crystal temperature for the case of AlN. The bulk ionized impurity concentration, $N_T$ , is set to $10^{17} \text{ cm}^{-3}$ . The electron concentration, $n$ , is set to the bulk ionized impurity concentration, $N_T$ . . . . .	68
4.16	The combined low-field electron drift mobility as a function of the crystal temperature for the case of AlN. The contributions to the low-field electron drift mobility considered include those related to the ionized impurity, polar optical phonon, piezoelectric, and acoustic deformation potential scattering mechanisms. For all cases, the electron concentration, $n$ , is set to the bulk ionized impurity concentration, $N_T$ . . . . .	69
4.17	The ionized impurity contribution to the low-field electron drift mobility as a function of the crystal temperature for the case InN. For all cases, the electron concentration, $n$ , is set to the bulk ionized impurity concentration, $N_T$ . . . . .	71
4.18	The polar optical phonon contribution to the low-field electron drift mobility as a function of the crystal temperature for the case of InN. . . . .	72
4.19	The piezoelectric contribution to the low-field electron drift mobility as a function of the crystal temperature for various selections of the electron concentration for the case of InN. . . . .	74

*List of Figures*

---

4.20	The acoustic deformation potential contribution to the low-field electron drift mobility as a function of the crystal temperature for the case of InN. . . . .	75
4.21	The polar optical phonon, piezoelectric, and acoustic deformation potential contributions to the low-field electron drift mobility, and the combined low-field electron drift mobility, plotted as functions of the crystal temperature for the case of InN. For the purposes of this analysis, the ionized impurity contribution is neglected, i.e., it is set to infinity. The electron concentration, $n$ , is set to $10^{17} \text{ cm}^{-3}$ for all cases. . .	77
4.22	The combined low-field electron drift mobility as a function of the crystal temperature with the polar optical phonon, piezoelectric, and acoustic deformation potential scattering mechanisms taken into account for various electron concentrations for the case of InN. For all cases, the ionized impurity contribution is neglected, i.e., it is set to infinity. . . . .	78
4.23	The ionized impurity, polar optical phonon, piezoelectric, and acoustic deformation potential contributions to the low-field electron drift mobility as a function of the crystal temperature for the case of InN. The bulk ionized impurity concentration, $N_T$ , is set to $10^{17} \text{ cm}^{-3}$ . The electron concentration, $n$ , is set to the bulk ionized impurity concentration, $N_T$ . . . . .	80

*List of Figures*

---

4.24	The combined low-field electron drift mobility as a function of the crystal temperature for the case of InN. The contributions to the low-field electron drift mobility considered include those related to the ionized impurity, polar optical phonon, piezoelectric, and acoustic deformation potential scattering mechanisms. For all cases, the electron concentration, $n$ , is set to the bulk ionized impurity concentration, $N_T$ . . . . .	81
4.25	The ionized impurity contribution to the low-field electron drift mobility as a function of the crystal temperature for the case ZnO. For all cases, the electron concentration, $n$ , is set to the bulk ionized impurity concentration, $N_T$ . . . . .	82
4.26	The polar optical phonon contribution to the low-field electron drift mobility as a function of the crystal temperature for the case of ZnO. . . . .	84
4.27	The piezoelectric contribution to the low-field electron drift mobility as a function of the crystal temperature for various selections of the electron concentration for the case of ZnO. . . . .	85
4.28	The acoustic deformation potential contribution to the low-field electron drift mobility as a function of the crystal temperature for the case of ZnO. . . . .	87

*List of Figures*

---

4.29	The polar optical phonon, piezoelectric, and acoustic deformation potential contributions to the low-field electron drift mobility, and the combined low-field electron drift mobility, plotted as functions of the crystal temperature for the case of ZnO. For the purposes of this analysis, the ionized impurity contribution is neglected, i.e., it is set to infinity. The electron concentration, $n$ , is set to $10^{17} \text{ cm}^{-3}$ for all cases. . .	88
4.30	The combined low-field electron drift mobility plotted as a function of the crystal temperature with the polar optical phonon, piezoelectric, and acoustic deformation potential scattering mechanisms taken into account for various electron concentrations for the case of ZnO. For all cases, the ionized impurity contribution is neglected, i.e., it is set to infinity. . .	90
4.31	The ionized impurity, polar optical phonon, piezoelectric, and acoustic deformation potential contributions to the low-field electron drift mobility as a function of the crystal temperature for the case of ZnO. The bulk ionized impurity concentration, $N_T$ , is set to $10^{17} \text{ cm}^{-3}$ . The electron concentration, $n$ , is set to the bulk ionized impurity concentration, $N_T$ . . . . .	91

*List of Figures*

---

4.32	The combined low-field electron drift mobility as a function of the crystal temperature for the case of ZnO. The contributions to the low-field electron drift mobility considered include those related to the ionized impurity, polar optical phonon, piezoelectric, and acoustic deformation potential scattering mechanisms. For all cases, the electron concentration, $n$ , is set to the bulk ionized impurity concentration, $N_T$ . . . . .	92
4.33	The combined low-field electron drift mobility dependence on the crystal temperature for the cases of GaN, AlN, InN, and ZnO. For cases, the bulk ionized impurity is set to $10^{17} \text{ cm}^{-3}$ . For all cases, the electron concentration, $n$ , is set to the bulk ionized impurity concentration, $N_T$ . . . . .	94
4.34	The combined low-field electron drift mobility as a function of the crystal temperature for the case of GaN for various electron concentrations. The bulk ionized impurity concentration, $N_T$ , is set to $10^{17} \text{ cm}^{-3}$ for all cases. . . . .	96
4.35	The combined low-field electron drift mobility as a function of the crystal temperature for the case of AlN for various electron concentrations. The bulk ionized impurity concentration, $N_T$ , is set to $10^{17} \text{ cm}^{-3}$ for all cases. . . . .	97
4.36	The combined low-field electron drift mobility as a function of the crystal temperature for the case of InN for various electron concentrations. The bulk ionized impurity concentration, $N_T$ , is set to $10^{17} \text{ cm}^{-3}$ for all cases. . . . .	98

*List of Figures*

---

4.37 The combined low-field electron drift mobility as a function of the crystal temperature for the case of ZnO for various electron concentrations. The bulk ionized impurity concentration,  $N_T$ , is set to  $10^{17}\text{cm}^{-3}$  for all cases. . . . . 99

# Acknowledgements

I would like to thank Dr. Stephen O’Leary, my advisor during the course of my studies, with whom this ambition for my life could not have been fulfilled. I would also like to thank my committee members, Drs. Jonathan Holzman and Julian Cheng, for giving invaluable input during the course of my research, and for providing me with support along the way. In addition, I would like to thank my friends for their encouragement and support which made my graduate experience a memorable one. This thesis is dedicated to my parents, Sri. Anand Babu Cheekoori and Smt. Vijaya Kumari Cheekoori, whose love, prayers, and faith in me have led me thus far and will continue to take me through the rest of my life.

# Chapter 1

## Introduction

The electronics age found its genesis with the development of the first transistor in 1947 [1]. Much of the progress that has occurred in electronics since that time has arisen as a result of making the electron devices within electronic systems smaller, faster, cheaper, and more reliable. These advances have occurred as a result of a detailed and quantitative understanding of the material properties of the materials used within electron devices. Electron devices are comprised of conductors, insulators, and semiconductors. While the material properties of conductors and insulators have been well understood for many years, the material properties of semiconductors were relatively unknown until the development of the electronics industry. Prior to that time, semiconductors were considered a laboratory curiosity.

Further progress in electronics will undoubtedly require further research into the material properties of the semiconductors used within electron devices. Since the 1950s, crystalline silicon (c-Si) has served as the dominant semiconductor within the electronics industry. Although c-Si possesses an indirect energy gap, its popularity stems from the fact that it is inexpensive to manufacture and is widely available [2]. At the present moment, c-Si is used in a variety of electron device configurations, including rectifiers,

metal-oxide-semiconductor field effect transistors, bipolar junction transistors, and thyristors [3]. The dominant role that c-Si plays in the electronics industry is unlikely to change in the near-term future.

Unfortunately, the energy gap of c-Si is narrow, i.e., 1.12 eV at room temperature [4]. This limits the range of electron device applications that can employ this material. At high temperatures, i.e., temperatures beyond 200 °C, the intrinsic electron concentration associated with c-Si exceeds desired levels; the intrinsic electron concentrations, corresponding to c-Si, crystalline germanium (c-Ge), and crystalline gallium arsenide (c-GaAs), are depicted as a function of the reciprocal temperature in Figure 1.1. At 300 °C, for example, it is noted that the intrinsic electron concentration associated with c-Si is found to be in excess of  $10^{15}$  cm<sup>-3</sup>. As a consequence, the doping levels required for the realization of p-n junction based electron devices simply can not be achieved. Accordingly, alternate semiconductor materials, with wider energy gaps, and hence, lower intrinsic electron concentrations, must be considered instead for high-temperature electron device applications [5].

The energy gap associated with a semiconductor corresponds to the energy difference between the top of the valence band and the bottom of the conduction band; the energy gap is depicted in Figure 1.2. At zero temperature, the valence band is fully occupied and the conduction band is completely unoccupied. If an electron within the valence band acquires sufficient energy, through the absorption of a photon or through thermal processes, it can transition into the conduction band. Accordingly, the energy gap associated with a semiconductor plays an important role in determining the ma-

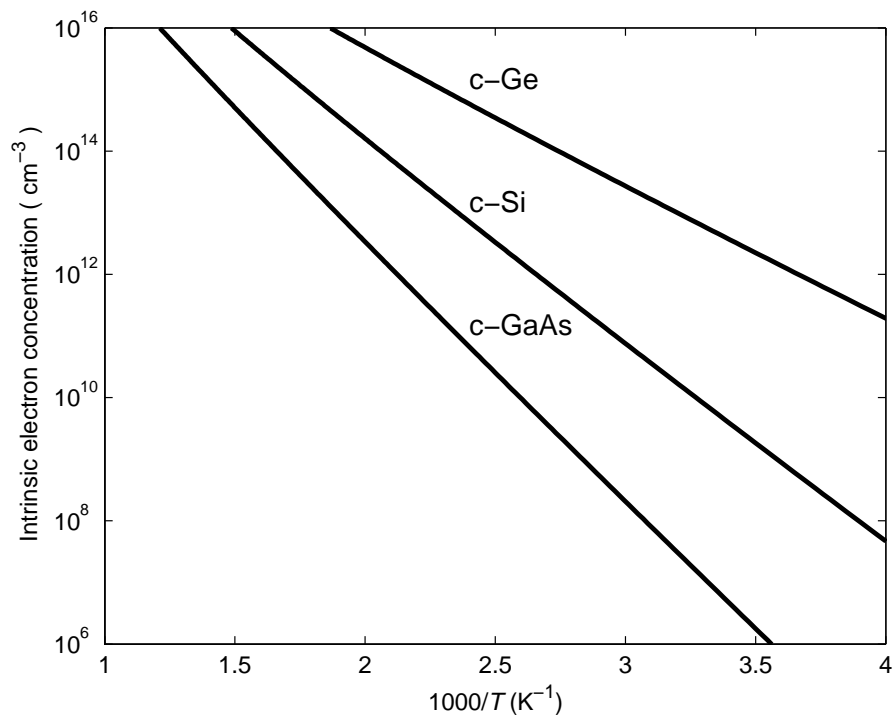


Figure 1.1: The intrinsic electron concentrations, for c-Si, c-Ge, and c-GaAs, as a function of the reciprocal temperature.

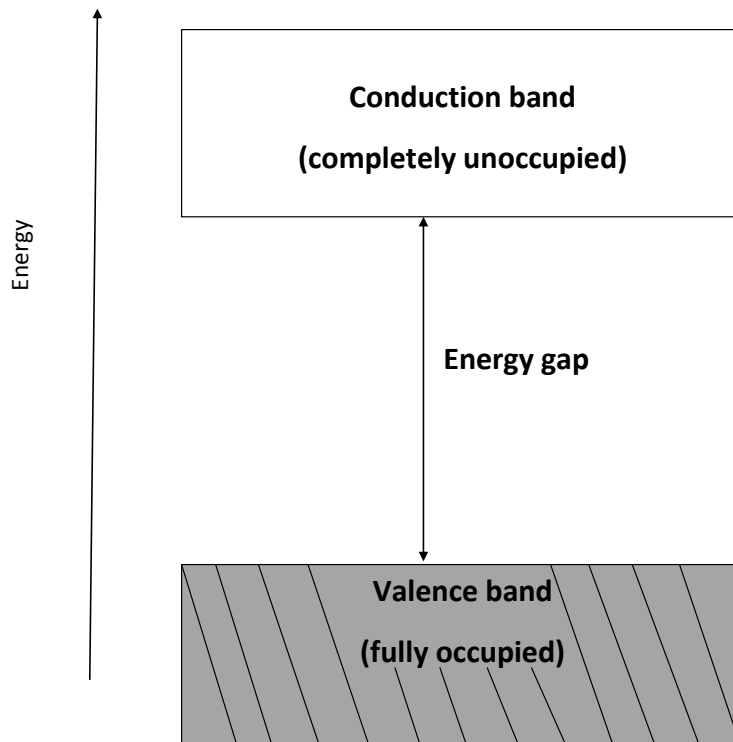


Figure 1.2: The energy gap represents the difference in energy between top of the valence band and the bottom of the conduction band. At zero temperature, the valence band is fully occupied and the conduction band is completely unoccupied.

terial properties of the semiconductor [6]. The energy gaps associated with naturally occurring semiconductors range from 0.17 to 6.2 eV [5, 7]. The energy gaps associated with a number of elemental and compound semiconductors are depicted in Figure 1.3 [8]. Wide energy gap semiconductors are generally referred to as those that exhibit energy gaps in excess of 2 eV [5].

Interest in wide energy gap semiconductors has been considerable in recent years. In addition to offering lower intrinsic electron concentrations, wide energy gap semiconductors offer a number of other favourable material properties, including higher electric breakdown fields and higher thermal conductivities. In addition, many of the wide energy gap semiconductors possess direct energy gaps, making them useful for a variety of opto-electronic device applications; as c-Si possesses an indirect energy gap, opto-electronic device applications using this material are not possible. A few of the more important wide energy gap semiconductors include gallium nitride (GaN), with a direct energy gap of 3.39 eV at room temperature [9], aluminium nitride (AlN), with a direct energy gap of 6.2 eV at room temperature [10], zinc oxide (ZnO), with a direct energy gap of 3.4 eV [11] at room temperature, and zinc selenide (ZnSe), with a direct energy gap of 2.7 eV at room temperature.

The performance of an electron device is often related to the transport of the charge carriers within the device. The transport of charge carriers depends on a variety of factors, including the crystal temperature, the electron concentration, and the impurities that are present. The charge transport that occurs is often characterized in terms of the dependence of the electron drift velocity on the applied electric field, i.e.,  $v_e(\mathcal{E})$ , where  $v_e$

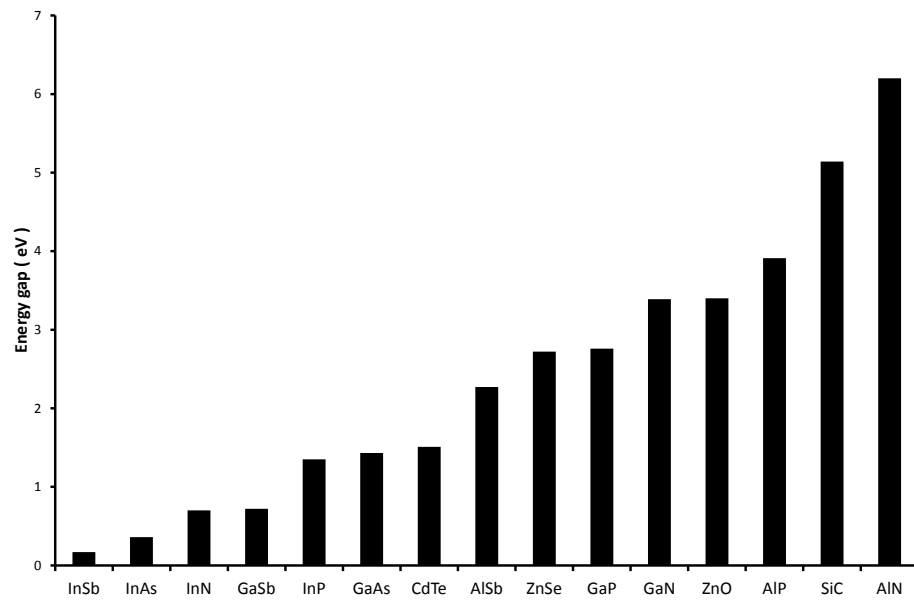


Figure 1.3: The room temperature energy gaps associated with a variety of compound semiconductors. The data depicted in this figure is from Adachi [8].

denotes the electron drift velocity and  $\mathcal{E}$  represents the applied electric field. The velocity-field characteristic, as this dependence is usually referred to as, plays an important role in determining the transport of the charge carriers within semiconductors, and, as a consequence, its determination is a central goal of studies into the material properties of semiconductors. The 300 K velocity-field characteristic associated with c-Si is contrasted with that associated with c-GaAs in Figure 1.4.

The low-field electron drift mobility,  $\mu_e$ , corresponds to the slope of the electron velocity-field characteristic at zero applied electric field, i.e.,

$$\mu_e = \left. \frac{dv_e(\mathcal{E})}{d\mathcal{E}} \right|_{\mathcal{E}=0}. \quad (1.1)$$

While not as informative as the velocity-field characteristic itself, the low-field electron drift mobility plays an important role in shaping the performance of many electron devices, as many devices operate at low applied electric fields. Indeed, for low applied electric fields, the non-linearities found in the full velocity-field characteristic do not play a role in shaping the corresponding device performance. It is this low-field electron drift mobility,  $\mu_e$ , that will be the focus of the subsequent work presented in this thesis.

In this thesis, how the low-field electron drift mobility,  $\mu_e$ , associated with a number of wide energy gap semiconductors, varies with the crystal temperature, the doping concentration, and the charge carrier concentration, will be examined. Initially, the analysis will focus on the contributions to the low-field electron drift mobility associated with some of the more important underlying scattering mechanisms, including ionized impurity scat-

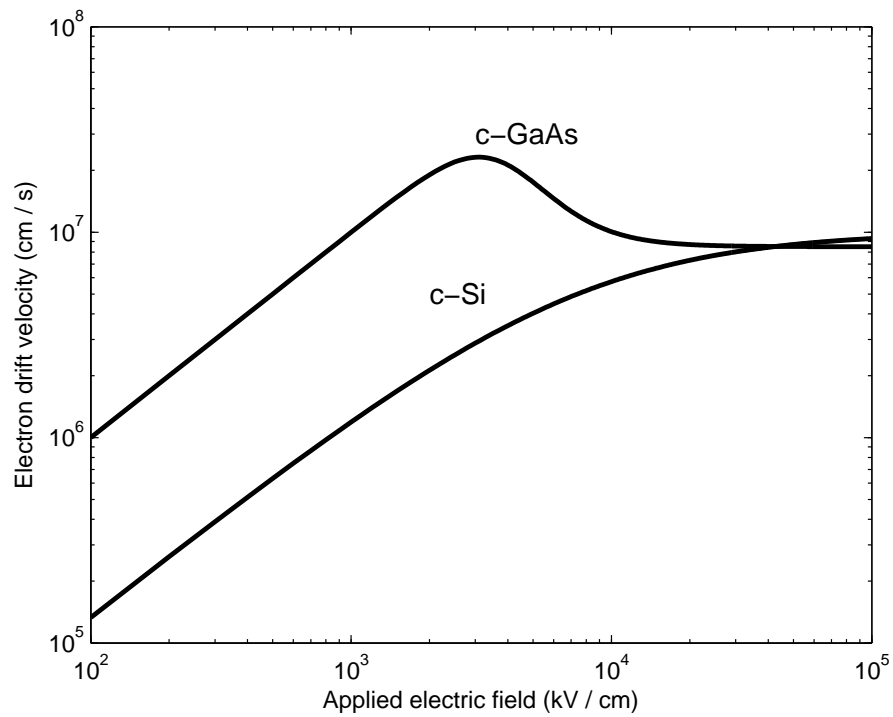


Figure 1.4: The velocity-field characteristics associated with c-Si and c-GaAs. Logarithmic scales are employed for both axes. For both cases, the crystal temperature is set to 300 K.

tering, polar optical phonon scattering, piezoelectric scattering, and acoustic deformation potential scattering. This analysis will be performed for bulk materials. Then, the role that the electron concentration plays in determining the low-field electron drift mobility associated with electrons confined within a two-dimensional electron gas will be studied, this configuration being representative of that found in many electron device configurations. The wide energy gap semiconductors considered in this analysis will include GaN, AlN, and ZnO. As indium nitride (InN), with a direct energy gap of 0.7 eV at room temperature [7], may be alloyed with GaN, and, as it is a semiconductor material of considerable current interest, InN will also be the focus of this analysis; while InN is not a wide energy gap semiconductor in of itself, alloys of InN with GaN are.

This thesis is organized in the following manner. In Chapter 2, the material properties of a number of wide energy gap semiconductors are presented. Then, in Chapter 3, expressions for the various contributions to low-field electron drift mobility will be provided. The analysis of the low-field electron drift mobility associated with GaN, AlN, InN, and ZnO will then be discussed in Chapter 4. The impact that electron concentrations play in determining the low-field electron drift mobility of the electrons confined within a two-dimensional electron gas will also be examined in Chapter 4. Finally, conclusions and recommendations for further study are presented in Chapter 5.

## Chapter 2

# Material properties

### 2.1 Material properties and electron device performance

The performance of an electron device may be determined from the material properties of the semiconductors found within the device. Accordingly, interest in the material properties of semiconductors have been the focus of great attention since the dawn of the electronics revolution more than half a century ago. With the dimensions of modern electron devices approaching fundamental quantum limits, researchers are currently seeking means of bypassing these limits. These efforts have, thus far anyway, focused on the material properties of semiconductors at the atomic level. Thus, current interest in the material properties of semiconductors is intense. This interest seems likely to continue for the foreseeable future.

In this chapter, the material properties of semiconductors will be examined. The focus of this examination will be on material properties that directly relate to the low-field electron drift mobility,  $\mu_e$ . The analysis will begin, however, with a description of the energy levels of the electrons within materials. The relationship between the distributions of electronic states

and the energy gap will then be featured, this allowing one to qualitatively understand the differences between conductors, insulators, and semiconductors. Following these preliminaries, the dependence of a number of key material properties on the energy gap will be presented, some of the materials considered being those that will be subsequently studied.

This chapter is organized in the following manner. In Section 2.2, the distribution of electronic states within a semiconductor is described. Then, in Section 2.3, the difference between indirect and direct energy gap semiconductors is discussed. The temperature dependence of the energy gap is then examined in Section 2.4. In Section 2.5, wide energy gap semiconductors are introduced. Finally, in Section 2.6, the dependence of the other material properties on the energy gap is examined for a wide variety of compound semiconductors.

## 2.2 The distribution of electronic states

Isolated atoms possess a discrete spectrum of allowed energy levels. Consider, for example, the case of the isolated carbon (C) atom. The discrete electron energy levels associated with this atom are depicted in Figure 2.1 [3]. Note that these electron energy levels are associated with the different orbital states that are present. The occupancy of these electronic states determines the properties of the material. The electronic structure, i.e., the states that are present and their occupancy, associated with the isolated C atom in the ground state, for example, may be succinctly expressed in the usual shorthand chemical nomenclature,  $1s^2 2s^2 2p^2$  [3].

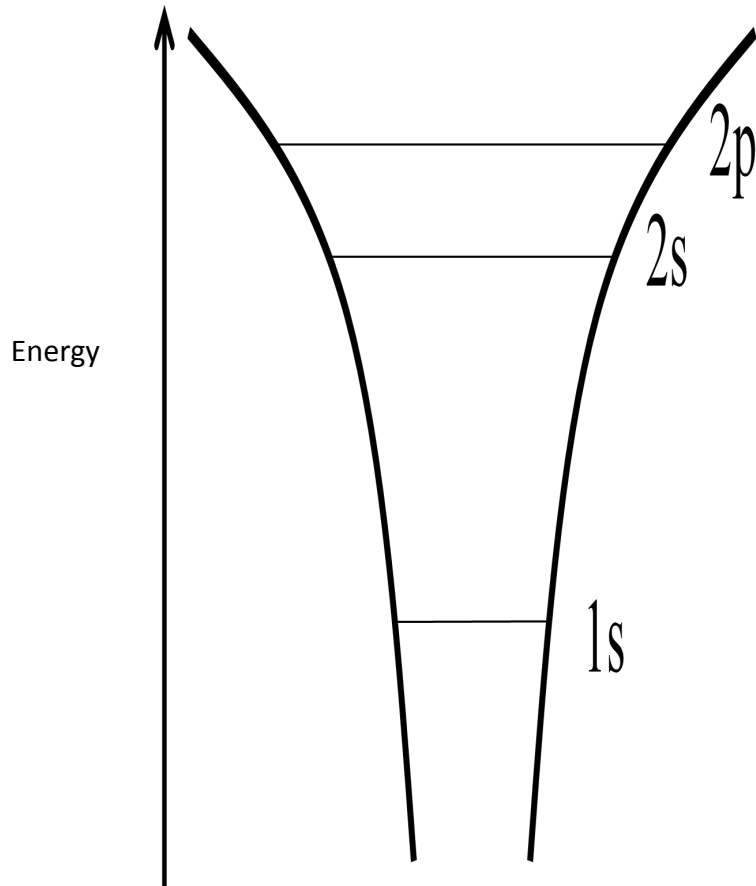


Figure 2.1: The electron energy levels associated with an isolated C atom. This figure is after Streetman [3].

## 2.2. The distribution of electronic states

---

As isolated atoms are brought together in order to form a solid, these discrete energy levels will broaden into bands. Consider the case of C, for example, as depicted in Figure 2.2 [3, 12]. For the case  $N$  C atoms at infinite inter-atomic separation, the isolated C atom energy levels appear. As the  $N$  C atoms are brought together, however, this discrete spectrum of energy levels will broaden into bands, the 2s and 2p energy levels being the first to broaden; the 1s energy levels will broaden at smaller inter-atomic separation distances, as these electrons correspond to the core electrons of the atom, i.e., their electron wave functions are more tightly bound to the atom than the 2s and 2p electron wave functions. The band associated with the 2p states will be comprised of  $6N$  states,  $2N$  of which are occupied. In contrast, the band associated with the 2s states will be comprised of  $2N$  states,  $2N$  of which are occupied. The band associated with the 1s states will be comprised of  $2N$  states,  $2N$  of which are occupied [3].

At sufficiently small inter-atomic spacings, the band associated with the 2s and 2p states will merge into a hybrid band, comprised of  $8N$  electronic states,  $4N$  of which will be occupied with electrons. Further reductions in the inter-atomic spacing will result in a split of this merged band into two bands, both with  $4N$  electronic states, separated by an energy gap,  $E_g$ . At zero temperature, the lower energy band, which is referred to as the valence band, is fully occupied, i.e., it will host  $4N$  electrons. In contrast, the upper energy band, which is referred to as the conduction band, is completely unoccupied, i.e., it will host no electrons. The energy difference between the valence band maximum and the conduction band minimum, at the equilibrium lattice spacing, is the energy gap. The energy gap,  $E_g$ ,

2.2. The distribution of electronic states

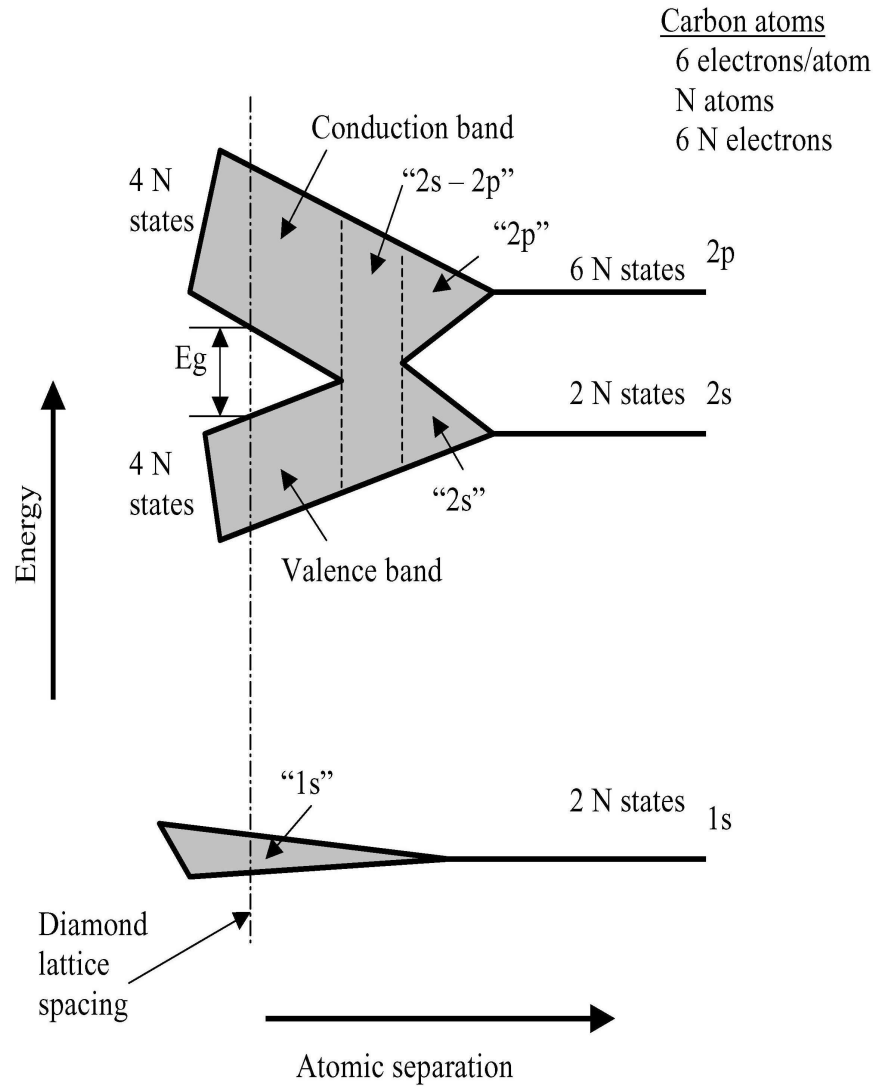


Figure 2.2: The formation of the energy gap within C. This figure is after Streetman [3]. This particular image is from Malik [12].

corresponding to c-Si maybe accounted for in a similar manner [3].

## 2.3 Direct and indirect energy gaps

The character of a band may be specified by determining how the electron energy levels vary as a function of the crystal momentum,  $\hbar k$ . These dependencies are usually specified through an energy band diagram, which plots the corresponding electron energy levels as a function of the crystal momentum,  $\hbar k$ , along critical lines of symmetry. Semiconductors for which the conduction band minimum does not occur at the same value of  $k$  as the valence band maximum, such as c-Si, are referred to as indirect energy gap semiconductors. In contrast, semiconductors for which the conduction band minimum occurs at the same value of  $k$  as the valence band maximum, such as c-GaAs, are referred to as direct energy gap semiconductors. One dimensional representations of the energy band diagrams associated with c-Si and c-GaAs are depicted in Figure 2.3 [3]. Direct energy gap semiconductors have better optical properties than their indirect counterparts. This is why c-Si is not used for opto-electronic device applications.

## 2.4 Temperature dependence of the energy gap

As the energy gap is an important parameter in the understanding of the material properties of a semiconductor, it has been the focus of much attention over the years. Detailed studies have demonstrated that the energy gap monotonically decreases with increases in the crystal temperature.

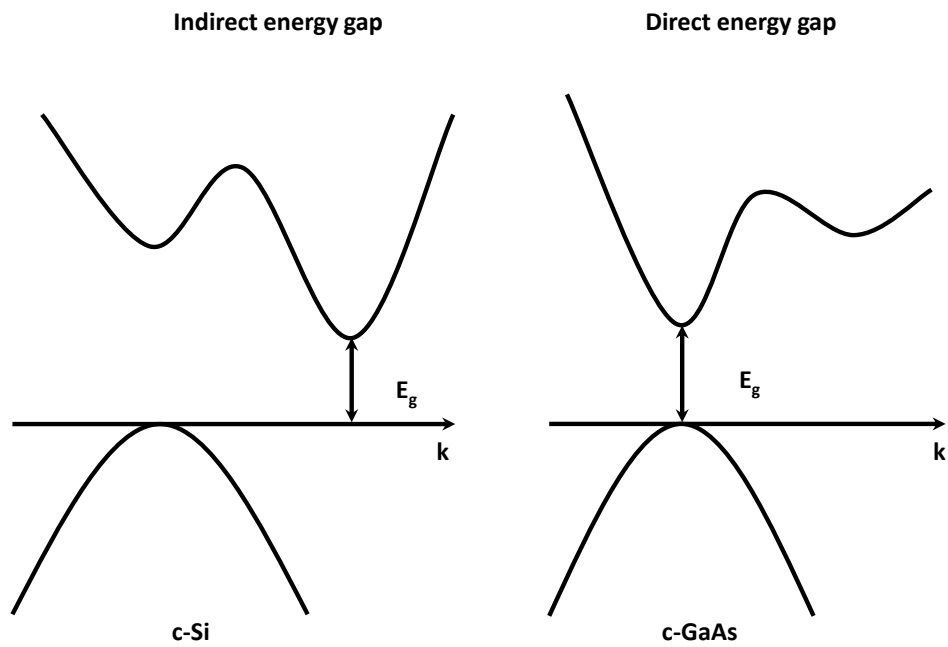


Figure 2.3: A one-dimensional depiction of the energy band diagrams associated with c-Si and c-GaAs. This figure is after Streetman [3].

Varshni [13] suggest that

$$E_g(T) = E_{g_o} - \frac{\alpha T^2}{T + \beta}, \quad (2.1)$$

where  $E_{g_o}$  denotes the energy gap at absolute zero and  $\alpha$  and  $\beta$  are empirically determined parameters that depend on the particular material being considered. For the case of c-Si, it is found that  $E_{g_o} = 1.169$  eV,  $\alpha = 4.9 \times 10^{-4}$  eV/K, and  $\beta = 655$  K, while for the case of c-GaAs, it is found that  $E_{g_o} = 1.519$  eV,  $\alpha = 5.4 \times 10^{-4}$  eV/K, and  $\beta = 204$  K [14]. The dependence of the energy gaps associated with c-Si and c-GaAs on the crystal temperature, as determined from Eq. (2.1) and the associated parameter values, is depicted in Figure 2.4. It is noted that the decrease in the energy gap corresponding to increased crystal temperatures is quite significant, c-GaAs losing in excess of 30% of its zero-temperature energy gap when the crystal temperature is set to 1000 K.

## 2.5 Wide energy gap semiconductors

Wide energy gap semiconductors are semiconductors that possess wide energy gaps. GaN, AlN, and ZnO, with room temperature energy gaps of 3.39, 6.2, and 3.4 eV, respectively, are referred to as wide energy gap semiconductors [5]. While the exact use of the term may be the subject of debate, there is general consensus that materials with energy gaps in excess of 2 eV may be referred to as wide energy gap semiconductors [5]. The energy gap differences, between a semiconductor and a wide energy gap semiconductor,

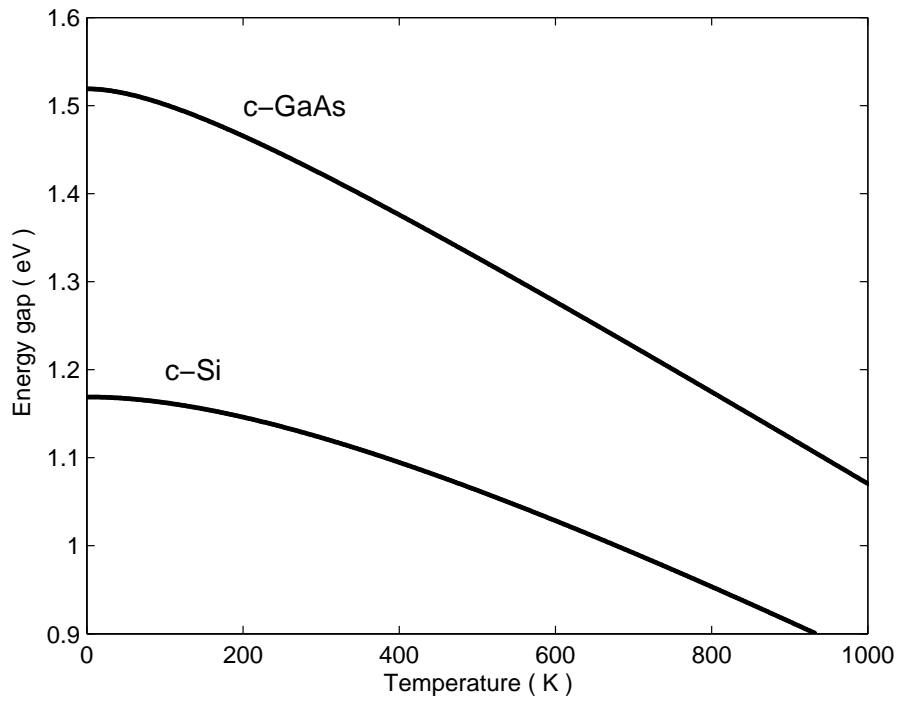


Figure 2.4: The energy gaps associated with c-Si and c-GaAs as a function of the crystal temperature. These plots are determined using the Varshni relationship, i.e., Eq. (2.1), for the empirical parameter selections suggested in the text.

## *2.6. Other material properties and their dependence on the energy gap*

---

are depicted are Figure 2.5. Recalling the energy gap tabulation provided in Figure 1.3, it is seen that there are a number of wide energy gap semiconductors that are available, including aluminium antimonide (AlSb), AlN, aluminium phosphide (AlP), GaN, gallium phosphide (GaP), silicon carbide (SiC), ZnO, and ZnSe.

## **2.6 Other material properties and their dependence on the energy gap**

The effective mass of a semiconductor is directly tied to its energy gap. In Figure 2.6, the electron effective mass is plotted as a function of the corresponding energy gap for a number of compound semiconductors. It is seen that the electron effective mass essentially scales linearly with the energy gap, both for indirect and direct energy gap semiconductors; deviations from an exact linear dependence are in evidence, however. As the low-field electron drift mobility scales with the reciprocal of the electron effective mass, it is clear that wider energy gaps will correspond to lower low-field electron drift mobilities. This is in accord with experimental observation.

The breakdown electric field is known to increase with the breadth of the energy gap. In Figure 2.7, the breakdown electric field is plotted as function of the energy gap for a number of compound semiconductors. As is expected, wider energy gaps correspond to higher breakdown fields. The fact that GaN, for example, exhibits a breakdown field of 2.6 MV/cm, while c-Si exhibits a breakdown field of 300 kV/cm, was one of the major reasons why interest in the wide energy gap semiconductors started in the first place.

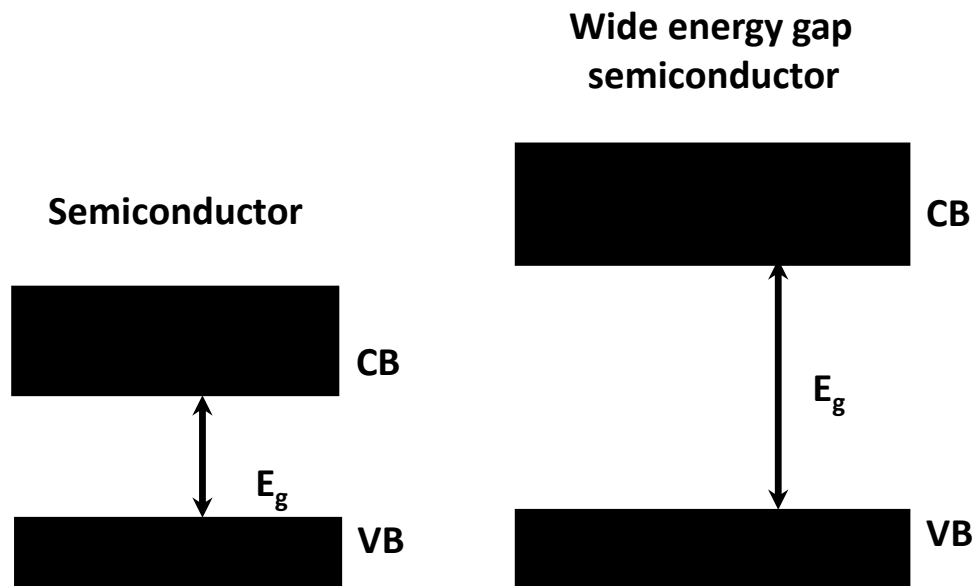


Figure 2.5: The differences in the energy gap between a semiconductor and a wide energy gap semiconductor

2.6. Other material properties and their dependence on the energy gap

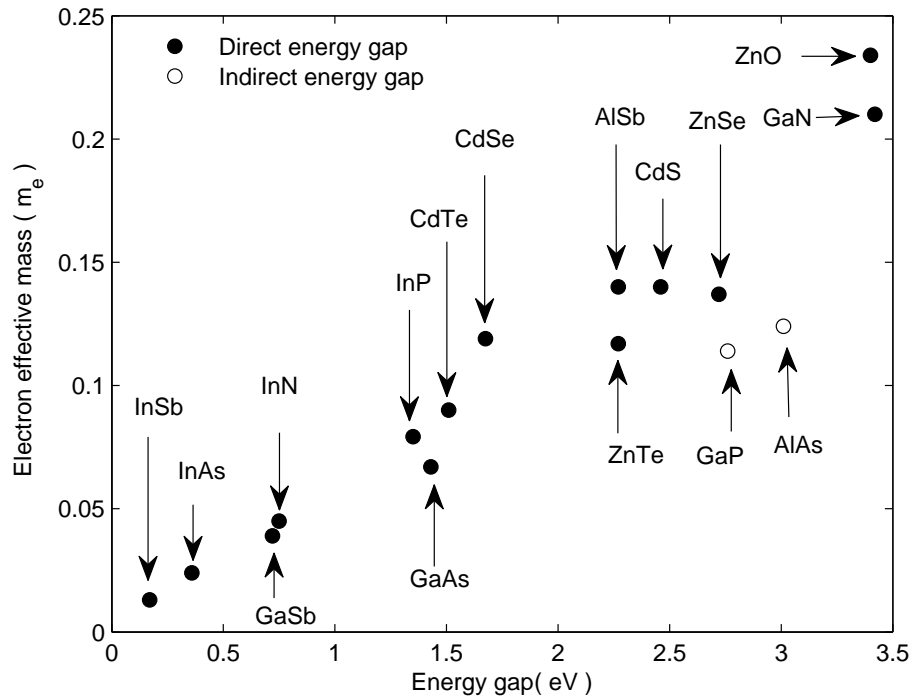


Figure 2.6: The electron effective mass as a function of the energy gap for selected III-V and II-VI semiconductors. The direct energy gap materials are depicted with the solid points, while the indirect energy gap materials are represented with the open points. Most of the data depicted in this figure is from Adachi [8]. The InN data, however, is from O’Leary *et al.* [15].

2.6. Other material properties and their dependence on the energy gap

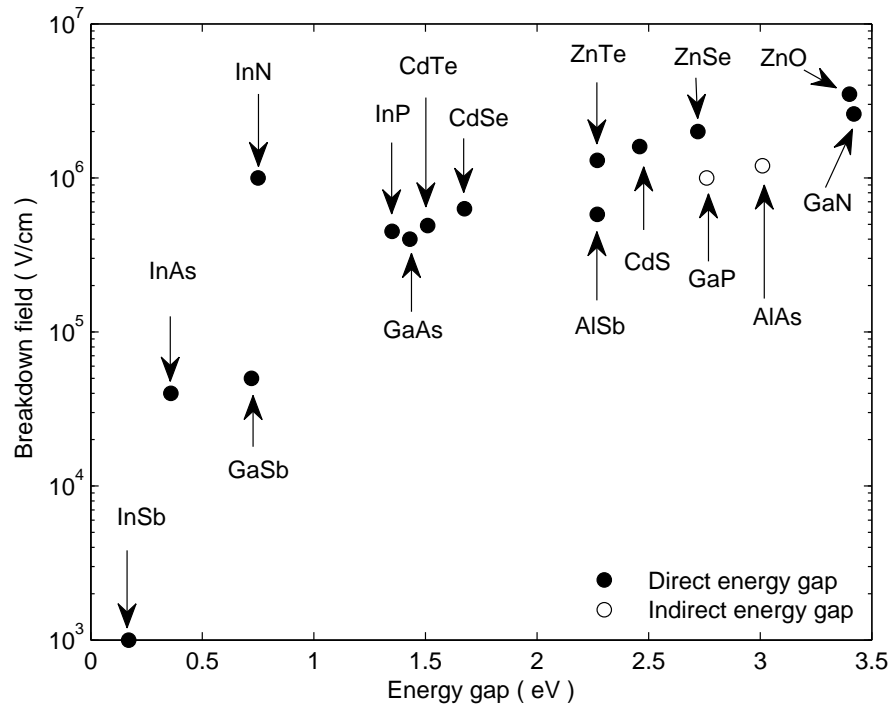


Figure 2.7: The breakdown electric field as a function of the energy gap for selected III-V and II-VI semiconductors. The direct energy gap materials are depicted with the solid points, while the indirect energy gap materials are depicted with the open points. The data depicted in this figure is from Adachi [8].

## 2.6. Other material properties and their dependence on the energy gap

---

Thus, GaN devices find applications in high-field settings. The same follows for other wide energy gap semiconductors.

The static and high frequency relative dielectric constants also vary with the energy gap. In Figure 2.8, the static relative dielectric constant,  $k_s = \epsilon_s/\epsilon_o$ , is plotted as a function of the energy gap for a number of compound semiconductors, where  $\epsilon_o$  denotes the dielectric function associated with free space. In Figure 2.9, the high-frequency relative dielectric constant,  $k_\infty = \epsilon_\infty/\epsilon_o$ , is plotted as a function of the energy gap for a number of compound semiconductors. It is seen that, in both cases, these optical constants diminish corresponding to increases in the energy gap. It is interesting to note that these relationships seem to cluster along two parallel lines, for the different compound semiconductors that are considered, both for the case of the static relative dielectric constant and for the case of the high-frequency relative dielectric constant. The reasons for this are unknown at present.

The electron affinity is also plotted as a function of the energy gap for the compound semiconductors considered in this analysis. This plot is depicted in Figure 2.10. It is seen that the electron affinity decreases in response to increases in the energy gap. This is likely arising as a consequence of the fact that large energy gap materials correspond to smaller energy differences between the vacuum level and the conduction band edge, thereby leading to reduced electron affinities.

2.6. Other material properties and their dependence on the energy gap

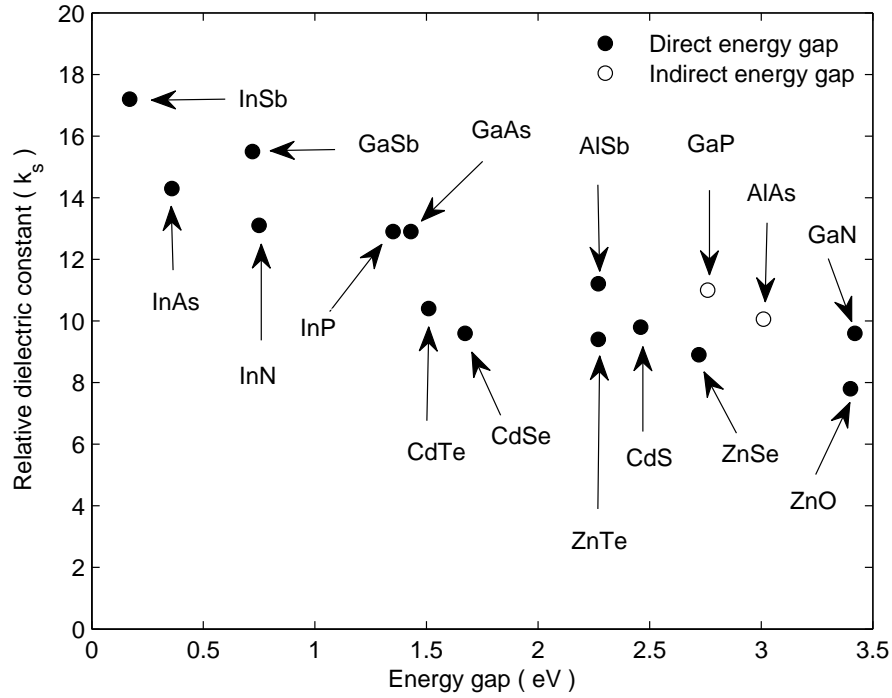


Figure 2.8: The static relative dielectric constant,  $k_s = \epsilon_s/\epsilon_0$ , as a function of the energy gap for selected III-V and II-VI semiconductors. The direct energy gap materials are depicted with the solid points, while the indirect energy gap materials are depicted with the open points. The data depicted in this figure is from Adachi [8].

2.6. Other material properties and their dependence on the energy gap

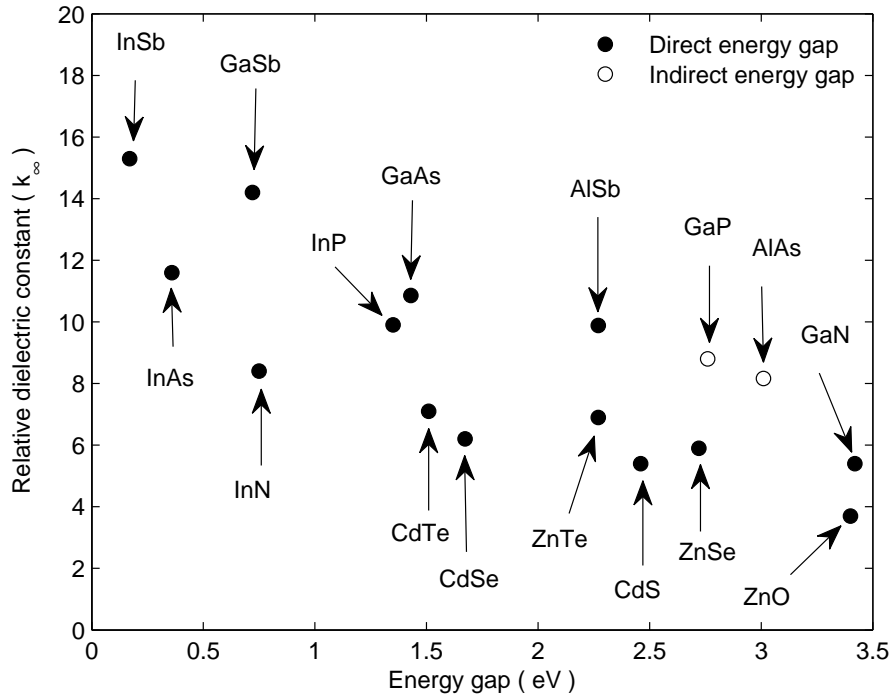


Figure 2.9: The high-frequency relative dielectric constant,  $k_\infty = \epsilon_\infty/\epsilon_0$ , as a function of the energy gap for selected III-V and II-VI semiconductors. The direct energy gap materials are depicted with the solid points, while the indirect energy gap materials are depicted with the open points. Most of the data depicted in this figure is from Adachi [8]. The InN data, however, is from O'Leary *et al.* [15].

2.6. Other material properties and their dependence on the energy gap

---

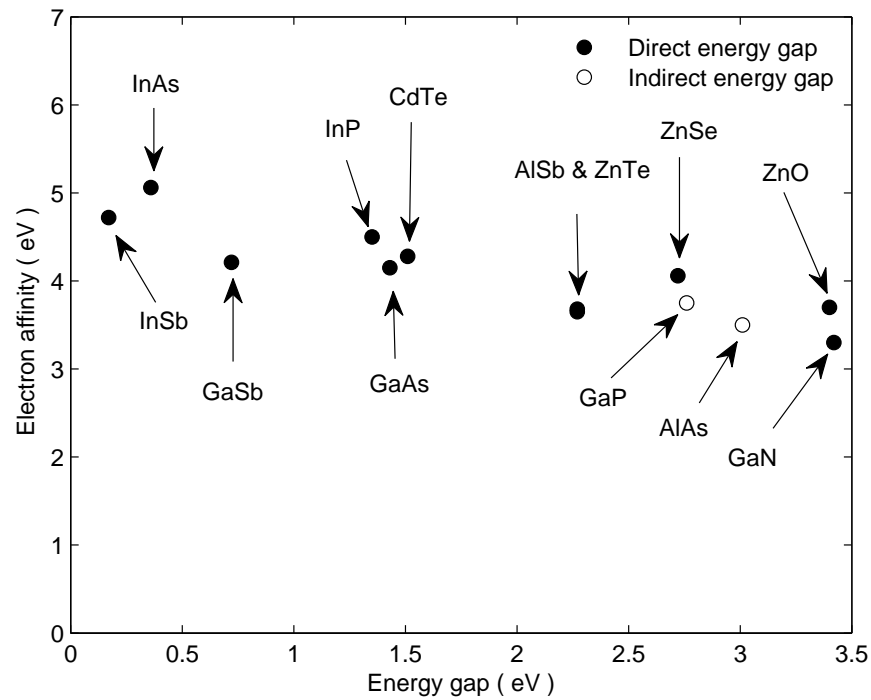


Figure 2.10: The electron affinity as a function of the energy gap for selected III-V and II-VI semiconductors. The direct energy gap materials are depicted with the solid points, while the indirect energy gap materials are depicted with the open points. The data depicted in this figure is from Adachi [8].

## Chapter 3

# Electron drift mobility in semiconductors

### 3.1 Electron drift mobility and scattering mechanisms

The low-field electron drift mobility,  $\mu_e$ , depends on the crystal temperature, the doping concentration, and the electron concentration. There are a variety of scattering processes that contribute to the low-field electron drift mobility. These include, but are not limited to, ionized impurity scattering, polar optical phonon scattering, piezoelectric scattering, and acoustic deformation potential scattering. In this thesis, the dependence of the low-field electron drift mobility,  $\mu_e$ , on crystal temperature, the doping concentration, and the electron concentration, corresponding to GaN, AlN, InN, and ZnO, will be examined for the case of bulk materials. The low-field electron drift mobility that occurs for the case of electrons in a confined two-dimensional electron gas, such as that that is present at the interface of a wide energy gap/narrow energy gap semiconductor discontinuity, is also evaluated for the case of these materials, deviations from the bulk results

### 3.2. *The random thermal motion of charge carriers in the absence of an applied electric field*

---

being the focus of this particular analysis.

This chapter is organized in the following manner. In Section 3.2, the motion of charge carriers within a semiconductor in the absence of an applied electric field is discussed. Then, in Section 3.3, how the charge carriers drift under the action of an applied electric field is considered. The different scattering mechanisms that the electrons will encounter during electron transport are then enumerated in Section 3.4. The drift mobilities associated with each of the different scattering mechanisms considered in this analysis, i.e., ionized impurity scattering, polar optical phonon scattering, piezoelectric scattering, and acoustic deformation potential scattering, are then presented, analytical expressions, corresponding to these drift mobilities, being provided in Section 3.5. Finally, in Section 3.6, means of analyzing the electron transport that occurs within a two-dimensional electron gas will be discussed.

## **3.2 The random thermal motion of charge carriers in the absence of an applied electric field**

In general, charge carriers within a semiconductor, i.e., electrons and holes, are generated and recombined. In thermal equilibrium, these processes are exactly balanced, i.e., the generation rate is exactly equal to the recombination rate. Before a charge carrier recombines, in the absence of an electric field, this charge carrier will randomly drift through the material. As

### 3.3. *Electron transport under the action of an applied electric field*

---

it drifts, it will be scattered through interactions with the various scattering mechanisms that are available. Scattering processes tend to randomize the direction that a charge carrier will propagate in. A representative random electron trajectory, corresponding to a particular individual electron in the ensemble of electrons that are available, is depicted in Figure 3.1 [3]. Holes also exhibit random trajectories in the absence of an applied electric field.

The electron drift velocity at any given time,  $t$ , corresponds to the average of the electron velocities over the entire ensemble of electrons. Focussing on the x-direction, if the  $i$ -th electron has a velocity,  $v_{xi}$ , in the x-direction, then the average velocity over the ensemble of electrons, or drift velocity, may be expressed as

$$v_{dx} \equiv \frac{1}{N}[v_{x1} + v_{x2} + v_{x3} + \cdots + v_{xN}]. \quad (3.1)$$

Given the randomness of the electron trajectories, as seen in Figure 3.1 [3], this velocity is nil in the absence of an applied electric field.

### **3.3 Electron transport under the action of an applied electric field**

If an electric field,  $\mathcal{E}$ , is applied, a net drift velocity will occur. Between scattering events, each electron will accelerate under the action of this applied electric field. Focussing on the motion of the  $i$ -th electron in the ensemble, if  $t = t_i$  is the time of the last scattering event that this particular electron has experienced, and if the applied electric field in the x-direction

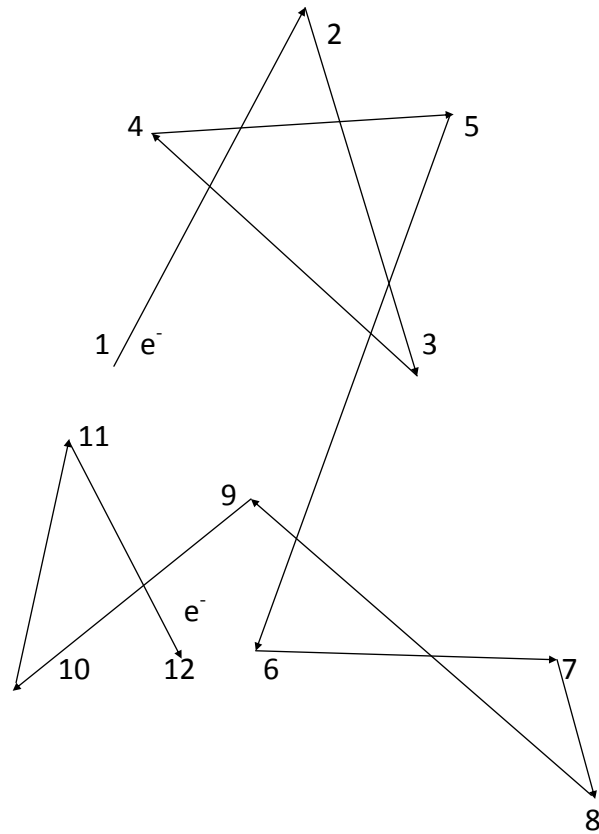


Figure 3.1: The random thermal motion of a representative electron in a semiconductor crystal in the absence of an applied electric field. This particular electron engages in scattering a number of times, the numbers 2 through 12 representing the scattering events that occur; number 1 corresponds to this particular electron's initial position. Between scattering events, the electron propagates with no acceleration. The scattering events are seen to randomize the direction of the electron transit. This figure is after Streetman [3].

### 3.3. Electron transport under the action of an applied electric field

---

is  $\mathcal{E}_x$ , then it can be shown that this particular electron's velocity at time  $t$  is

$$v_x^{(i)}(t) = -\frac{q\mathcal{E}_x}{m^*}(t - t_i) + v_x^{(i)}(t_i), \quad (3.2)$$

where  $q$  denotes the electron charge,  $m^*$  represents the electron effective mass, and  $v_x^{(i)}(t_i)$  denotes the velocity of this electron in the x-direction immediately following the last scattering event [14]. Averaging over the ensemble of electrons, i.e., using the definition in Eq. (3.1), it may be shown that

$$v_{dx} = -\frac{q\overline{(t - t_i)}}{m^*}\mathcal{E}_x, \quad (3.3)$$

where  $\overline{(t - t_i)}$  denotes the mean time between scattering events, a term which is henceforth denoted  $\tau$ . The low-field electron drift mobility,  $\mu_e$ , provides for the constant of proportionality between the electron drift velocity and the applied electric field. That is,

$$v_{dx} = -\mu_e\mathcal{E}_x, \quad (3.4)$$

where

$$\mu_e = \frac{q\tau}{m^*}. \quad (3.5)$$

If  $\lambda$  denotes the rate with which scattering processes interact with individual electrons, the mean time since the last scattering event,

$$\tau = \frac{1}{\lambda}. \quad (3.6)$$

### 3.3. Electron transport under the action of an applied electric field

---

Hence, the overall low-field electron drift mobility may be expressed as

$$\mu_e = \frac{q}{m^* \lambda}, \quad (3.7)$$

where  $q$ ,  $m^*$ , and  $\lambda$  are as previously defined.

It is instructive to introduce a low-field electron drift mobility,  $\mu_e$ , associated with each scattering process. For the  $j$ -th scattering process, with a scattering rate of  $\lambda^{(j)}$ , the  $j$ -th low-field electron drift mobility may be expressed as

$$\mu^{(j)} = \frac{q}{m^* \lambda^{(j)}}, \quad (3.8)$$

following the form presented in Eq. (3.7). As the overall scattering rate,  $\lambda$ , may be expressed as a sum over these individual rates, i.e.,

$$\lambda = \sum_{j=1}^N \lambda^{(j)}, \quad (3.9)$$

it is thus seen that

$$\mu_e = \frac{1}{\sum_{j=1}^N \frac{1}{\mu_e^{(j)}}}. \quad (3.10)$$

That is, the overall electron drift mobility corresponds to the reciprocal of the sum over the individual reciprocal low-field electron drift mobilities corresponding to the different scattering mechanisms. This overall electron drift mobility is henceforth referred to as the combined electron drift mobility. The remaining analysis presented in this chapter is focussed upon determining these individual contributions to the electron drift mobility.

### 3.4 Scattering mechanisms

As was discussed earlier, the low-field electron drift mobility,  $\mu_e$ , depends on a variety of different scattering mechanisms. The various scattering mechanisms, in their totality, are depicted in Figure 3.2 [8]. The transport of electrons within a semiconductor is usually characterized by an energy band diagram for the conduction band with a number of valleys, i.e., the actual energy band diagram is approximated by a series of valleys, the lowest energy valley corresponding to areas in the energy band diagram in the immediate vicinity of the conduction band minimum. In Figure 3.3 [16, 17], for example, a three-valley representation for the conduction band energy band diagram associated with c-GaAs is contrasted with the corresponding one-dimensional representation of the full energy band diagram.

There are important scattering mechanisms that occur, both within valleys, i.e., intravalley scattering mechanisms, and between valleys, i.e., intervalley scattering mechanisms. For the purposes of this analysis, the focus will be on the low-field electron drift mobility,  $\mu_e$ . As a result, intervalley scattering mechanisms will not be considered. The particular scattering processes that will be focus of this subsequent analysis are the ionized impurity scattering, polar optical phonon scattering, piezoelectric scattering, and acoustic deformation potential scattering mechanisms.

### 3.4. Scattering mechanisms

---

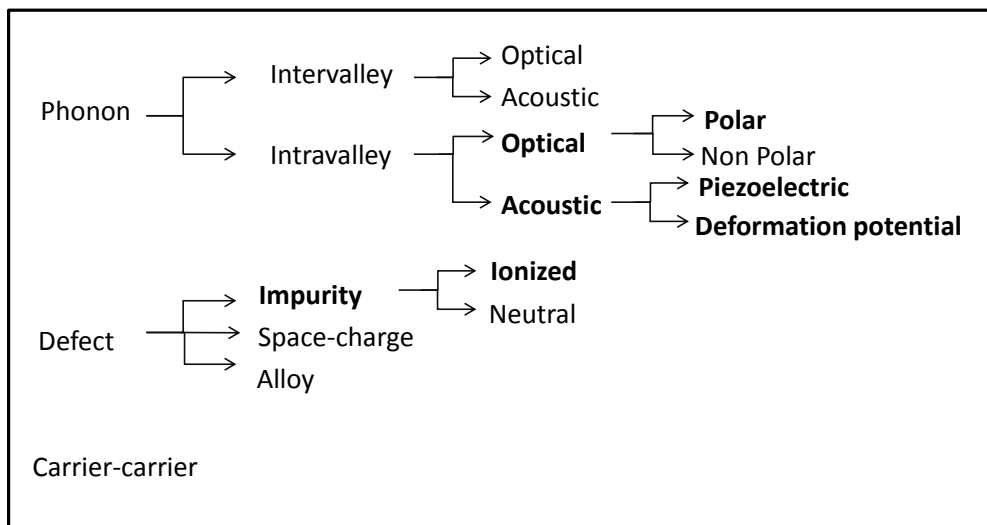


Figure 3.2: The different scattering mechanisms that can occur in semiconductors. The particular scattering mechanisms that we examine for the purposes of this analysis are presented with the bold font. This figure is after Adachi [8].

### 3.4. Scattering mechanisms

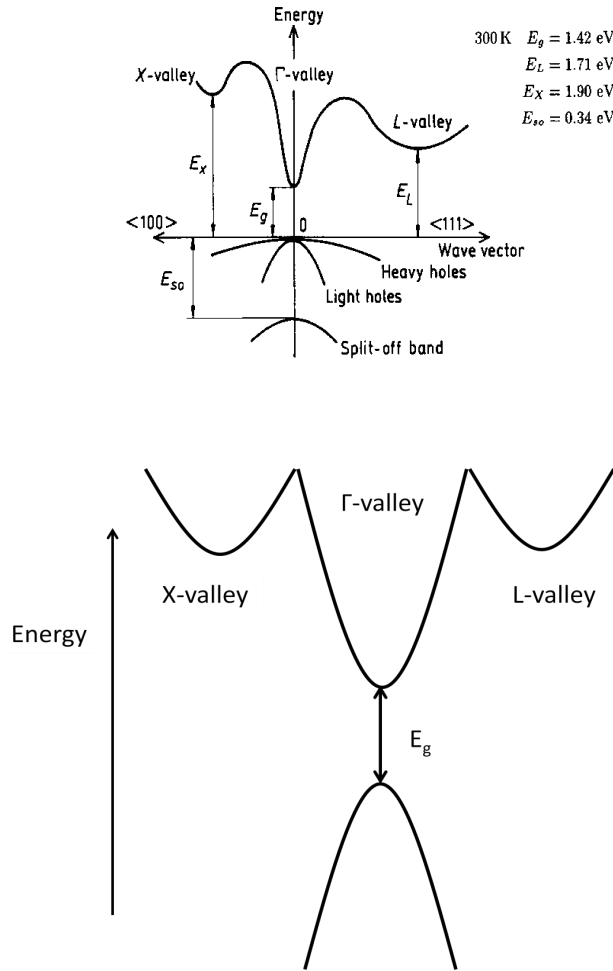


Figure 3.3: The energy band diagram associated with c-GaAs. A three-valley representation of this band diagram for the conduction band is depicted beneath a more exact one-dimensional representation of the energy band diagram corresponding to this material [16, 17].

## 3.5 Analytical expressions for the contributions to the low-field electron drift mobility

As was discussed earlier, the overall low-field electron drift mobility associated with a semiconductor may be related to the various scattering mechanisms that are present. For the purposes of this low-field electron drift mobility analysis, four scattering mechanisms will be considered, these being the dominant scattering mechanisms present at low applied electric fields, i.e., (1) ionized impurity scattering, (2) polar optical phonon scattering, (3) piezoelectric scattering, and (4) acoustic deformation potential scattering. The approach adopted will involve the determination of the electron drift mobility associated with each individual scattering mechanism, and the evaluation of a combined, i.e., overall, form of the electron drift mobility using Eq. (3.10).

### 3.5.1 Ionized impurity scattering

The impurities within a semiconductor play an important role in influencing the electron transport within these materials. Impurities are efficient scattering centres, especially when they are charged. Ionized donors or acceptors in a semiconductor are a common example of such impurities. The amount of scattering due to the electrostatic forces between the carriers and the ionized impurities depends on the interaction time and the concentration of impurities that are present. Higher impurity concentrations and greater interaction times result in a lower electron drift mobility. The dependence on the interaction time accounts for the crystal temperature dependence

### 3.5. Analytical expressions for the contributions to the low-field electron drift mobility

---

of the low-field electron drift mobility, i.e., greater crystal temperature results in a higher thermal electron velocity, which in turn leads to a reduced interaction time and therefore an enhanced low-field electron drift mobility.

The low-field electron drift mobility contribution corresponding to the ionized impurity scattering mechanism was shown by Shur *et al.* [18] to be

$$\mu_I = \frac{2^{5.5}\pi}{3} \varepsilon_s^2 \frac{(k_B T)^{3/2} F_3}{N_T q^3 m_n^{1/2} F_1}, \quad (3.11)$$

where

$$F_1 = \int_0^\infty \frac{x^{1/2}}{1 + \exp(x - e_F)} dx, \quad (3.12)$$

$$F_2 = \int_0^\infty \frac{x^{1/2} \exp(x - e_F)}{[1 + \exp(x - e_F)]^2} dx, \quad (3.13)$$

$$F_3 = \int_0^\infty \frac{x^3 \exp(x - e_F)}{\Phi_i [1 + \exp(x - e_F)]^2} dx, \quad (3.14)$$

$$\Phi_i = \ln(1 + \eta) - \frac{\eta}{1 + \eta}, \quad (3.15)$$

$$\eta = \frac{8m_n \varepsilon_s (k_B T)^2 F_1}{q^2 \hbar^2 n F_2} x, \quad (3.16)$$

and where  $\hbar$  denotes the reduced Planck's constant,  $q$  is the electron charge,  $m_n$  is the electron effective mass,  $\varepsilon_s$  is the static dielectric constant,  $N_T$  is the total concentration of ionized impurities, and  $n$  is the electron concentration.

### 3.5. Analytical expressions for the contributions to the low-field electron drift mobility

---

#### 3.5.2 Polar optical phonon scattering

Scattering by lattice waves involves the absorption or emission of polar optical phonons by the electrons within the ensemble. These phonons represent quanta of mechanical waves that travel through the semiconductor crystal. Since the density of phonons in a solid increases with the crystal temperature, the mean time between scattering events corresponding to this particular mechanism will decrease with increases in the crystal temperature. The low-field electron drift mobility contribution corresponding to the polar optical phonon scattering mechanism was shown by Shur *et al.* [18] to be

$$\mu_{\text{po}} = \frac{4\pi k \epsilon_o \hbar^2}{q N_p m_n} \frac{(1 - 5V_{\text{th}}/E_g)}{[2m_n q E_o (1 + E_o/E_g)]^{1/2}}, \quad (3.17)$$

where  $k = 1/(1/k_\infty - 1/k_s)$  is the coupling constant,  $k_\infty = \epsilon_\infty/\epsilon_o$  and  $k_s = \epsilon_s/\epsilon_o$  denoting the high frequency and static relative dielectric constants, respectively,  $\epsilon_o$  being the dielectric constant associated with free space,

$$N_p = 1/[\exp(E_o/V_{\text{th}}) - 1], \quad (3.18)$$

being Planck's function, representing the occupancy of the phonon states,  $V_{\text{th}} = k_B T/q$  is the thermal voltage,  $E_o$  is the polar optical phonon energy, and  $E_g$  is the energy gap.

#### 3.5.3 Piezoelectric scattering

Piezoelectric scattering occurs as a consequence of the acoustic wave vibrations through the piezoelectric effect. If the atoms in the semiconduc-

### 3.5. Analytical expressions for the contributions to the low-field electron drift mobility

---

tor crystal are partially ionized, and the displacement of the atoms due to acoustic vibrations produces an electric potential, piezoelectric scattering will occur. The magnitude of the piezoelectric scattering depends on the structure of the ionized atoms within the crystal. The magnitude of the piezoelectric scattering will be larger in crystals with lower symmetry. The scattering of electrons through the piezoelectric potential is referred to as piezoelectric scattering. Piezoelectric scattering plays an important role in compound semiconductors, particularly at low crystal temperatures. The low-field electron drift mobility contribution corresponding to the piezoelectric scattering mechanism was shown by Shur *et al.* [18] to be

$$\mu_p = \frac{q\tau_p}{m^*}, \quad (3.19)$$

where

$$\tau_p = \frac{2\pi\hbar^2\epsilon_s v_1}{q^2 K_{av}^2 k_B T} \frac{2F_p}{3F_1}, \quad (3.20)$$

$$F_p = \int_0^\infty \frac{x^2 \exp(x - e_F)}{F_{pz} [1 + \exp(x - e_F)]^2} dx, \quad (3.21)$$

and

$$F_{pz} = 1 + \frac{1}{1 + \eta} - \frac{2\ln[1 + \eta]}{\eta}. \quad (3.22)$$

$F_1$  is as defined in Eq. (3.12) and  $\eta$  is as defined in Eq. (3.16). Here, the electromechanical coefficient

$$K_{av}^2 = \frac{e_{14}^2(12/c_L + 16/c_T)}{35\epsilon_s}, \quad (3.23)$$

### 3.5. Analytical expressions for the contributions to the low-field electron drift mobility

where  $c_L$  and  $c_T$  denote the longitudinal and transverse elastic constants, respectively,  $e_{14}$  is the piezoelectric constant,  $\varepsilon_s$  is the static dielectric constant, and  $v_1$  is the thermal velocity, i.e.,  $v_1 = (2k_B T/m_n)^{1/2}$ .

#### 3.5.4 Acoustic phonon deformation potential scattering

The thermal energy within a semiconductor material leads to fluctuations in the location of the atomic positions with time. These acoustic waves, as such vibrations are commonly referred to as, lead to deformations in the material, an electrostatic potential being associated with these deformations. Shur *et al.* [18] demonstrate that the contribution to the low-field electron drift mobility associated with acoustic deformation potential scattering

$$\mu_{ac} = \frac{\sqrt{8\pi} q \hbar^4 c_L}{3E_1^2 m_n^{5/2} (k_B T)^{3/2}}, \quad (3.24)$$

where  $c_L$  is the longitudinal elastic constant of the semiconductor,  $E_1$  is the displacement of the band edge per unit dilation of the lattice, i.e., it is the deformation potential, and  $m_n$  is the electron effective mass. It is seen from Eq. (3.24) that  $\mu_{ac}$  is inversely proportional to a polynomial function of the electron effective mass and the crystal temperature. Increased crystal temperatures increase the intensity of the lattice vibrations that occur, and thus, the mean free time between the scattering events decreases, i.e., the mobility decreases. Thus, acoustic deformation potential scattering plays an important role, particularly at high temperatures[19].

### 3.6 Electron transport in a two-dimensional electron gas

At a heterojunction, such as the AlGa<sub>N</sub>/Ga<sub>N</sub> interface in a high-frequency field effect transistor configuration [20], a discontinuity in the potential energy associated with the conduction band is found, as is shown in Figure 3.4 [20]. When the band bending that occurs in a real device is taken into account, the resultant potential profile is as shown in this figure. Electron from the bulk AlGa<sub>N</sub> and Ga<sub>N</sub> layers will pour into the two-dimensional Ga<sub>N</sub> quantum well, thus producing a channel within which charge carrier conduction will occur. This Ga<sub>N</sub> channel is thus characterized with an electron concentration that far exceeds that of the corresponding bulk material. These extra free electrons will act to screen the underlying distribution of ionized impurity atoms within the channel, i.e., a two-dimensional electron gas is formed within this channel with an enhanced low-field electron drift mobility. This screening reduces the effect of the ionized impurity scattering. This in turn impacts upon the overall resultant electron transport characteristics.

A detailed and rigorous treatment of this problem is quite complex. The distribution of charge must be evaluated by simultaneously solving both Poisson's and Schrödinger's equations. This is beyond the scope of the present analysis. Instead, the strategy adopted here will be to examine how electron concentrations in excess of the bulk ionized impurity concentration, for a fixed bulk ionized impurity concentration, will impact upon the dependence of the low-field electron drift mobility on the crystal tempera-

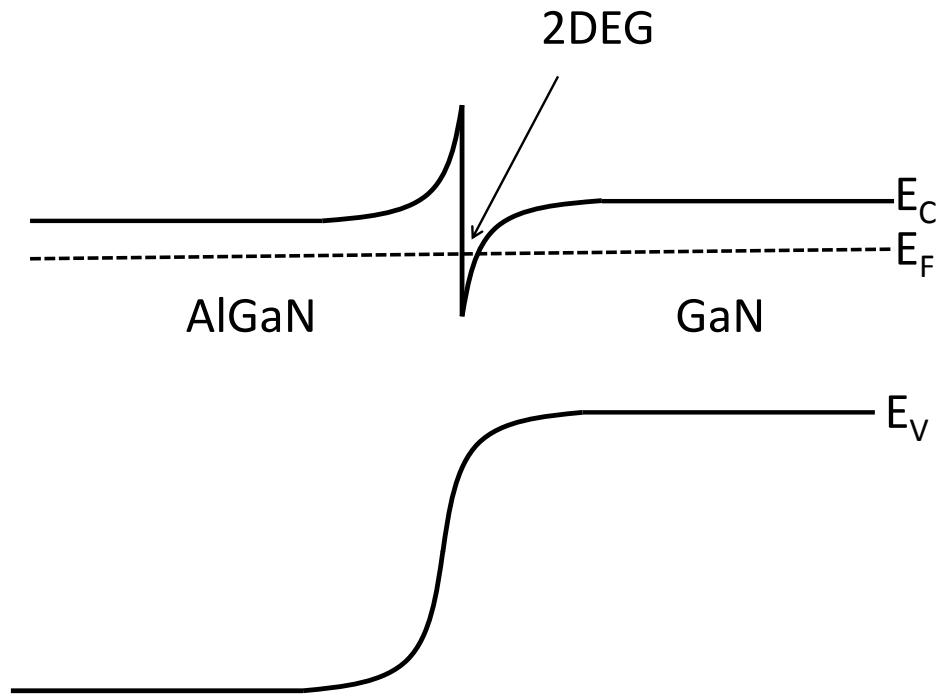


Figure 3.4: The energy band diagram of an AlGaN/GaN high electron mobility transistor. A quantum well is formed in the GaN layer close to the AlGaN/GaN interface. Mobile electrons, contributed from the AlGaN and GaN layers, are trapped in the quantum well that is present, thus forming a two-dimensional electron gas [20].

ture. In a bulk material at thermal equilibrium, charge neutrality mandates that the electron concentration,  $n$ , is exactly equal to the bulk ionized impurity concentration,  $N_T$ . In contrast, in the two-dimensional electron gas configuration, electron concentrations in excess of the bulk ionized impurity concentration are expected for the reasons suggested earlier. Thus, the adopted approach allows one to estimate the impact of the presence of a two-dimensional electron gas on the results within the framework of the already developed analysis. The additional electrons that are present in a two-dimensional electron gas contribute to increased screening. The increased screening that accompanies increased electron concentrations should allow for an increase in the resultant low-field electron drift mobility,  $\mu_e$ . The exact manner in which this occurs will be the focus of this analysis. The results of this analysis will be presented in Chapter 4.

# Chapter 4

## Results

### 4.1 Overview

The low-field electron drift mobility,  $\mu_e$ , is an important material property that provides a measure of the electron transport that occurs within a given material. The low-field electron drift mobility,  $\mu_e$ , provides an electron transport metric with which various materials can be compared and contrasted. At low-applied electric fields, the performance of a given electron device may be directly related to this parameter. The low-field electron drift mobility,  $\mu_e$ , is known to be a strong function of the crystal temperature, the doping concentration, and the electron concentration. Establishing how this low-field electron drift mobility depends on these parameters is an important goal in the characterization of any semiconductor. From this dependence, the suitability of an electronic material for a particular electron device configuration may be assessed.

In this chapter, the dependence of the low-field electron drift mobility,  $\mu_e$ , on the crystal temperature, the doping concentration, and the electron concentration, will be examined for the cases of GaN, AlN, InN, and ZnO. The expressions presented in the previous chapter will be employed for the purposes of this analysis, the individual contributions to the low-

field electron drift mobility related to the ionized impurity, polar optical phonon, piezoelectric, and acoustic deformation potential scattering mechanisms being combined to yield an overall low-field electron drift mobility in the manner prescribed in Eq. (3.10). Initially, each of the materials will be considered individually. Later, comparisons between the different materials will be made. Finally, a contrast between results obtained corresponding to the case of a bulk semiconductor and the case of a confined two-dimensional electron gas within such a semiconductor will be presented.

This chapter is organized in the following manner. In Section 4.2, the material parameters, corresponding to bulk GaN, AlN, InN, and ZnO, are provided. Then, in Sections 4.3, 4.4, 4.5, and 4.6, the contributions to the low-field electron drift mobility attributed to the ionized impurity, polar optical phonon, piezoelectric, and acoustic deformation potential scattering mechanisms, corresponding to GaN, AlN, InN, and ZnO, respectively, are presented. A comparison between these different semiconductor materials is then presented in Section 4.7. Finally, in Section 4.8, the dependence of the low-field electron drift mobility on the crystal temperature for electrons in a two-dimensional electron gas, for the cases of GaN, AlN, InN, and ZnO, is considered.

## 4.2 Material parameter selections

The low-field electron drift mobility,  $\mu_e$ , is a strong function of the material properties. Accordingly, in order to perform this analysis, the material parameters, corresponding to GaN, AlN, InN, and ZnO, must be specified.

#### 4.2. Material parameter selections

---

In Tables 4.1 and 4.2, the material parameters corresponding to these different semiconductor materials are specified. The material parameters that are specified in these tables correspond to those that are important for low-field electron drift mobility determinations. These values are mostly from O’Leary *et al.* [15] and Albrecht *et al.* [21].

Table 4.1: The material parameters corresponding GaN, AlN, and InN. These parameter selections are from O’Leary *et al.* [15].

Parameter	GaN	AlN	InN
Longitudinal sound velocity (cm/s)	$6.56 \times 10^5$	$9.06 \times 10^5$	$6.24 \times 10^5$
Transverse sound velocity (cm/s)	$2.68 \times 10^5$	$3.70 \times 10^5$	$2.55 \times 10^5$
Acoustic deformation potential (eV)	8.3	9.5	7.1
Static dielectric constant	8.9	8.5	15.3
High-frequency dielectric constant	5.35	4.77	8.4
Effective mass ( $\Gamma_1$ valley)	0.20 $m_e$	0.48 $m_e$	0.045 $m_e$
Piezoelectric constant, $e_{14}$ (C/cm <sup>2</sup> )	$3.75 \times 10^{-5}$	$9.2 \times 10^{-5}$	$3.75 \times 10^{-5}$
Direct energy gap (eV)	3.39	6.2	0.75a
Optical phonon energy (meV)	91.2	99.2	89.0

### 4.3. GaN bulk results

Table 4.2: The material parameters corresponding to ZnO. The ZnO parameter selections are from Albrecht *et al.* [21].

Parameter	ZnO
Longitudinal sound velocity (cm/s)	$4.0 \times 10^5$
Transverse sound velocity (cm/s)	$2.7 \times 10^5$
Acoustic deformation potential (eV)	3.83
Static dielectric constant	8.2
High-frequency dielectric constant	3.7
Effective mass ( $\Gamma_1$ valley)	$0.17 m_e$
Piezoelectric constant, $e_{14}$ (C/cm <sup>2</sup> )	$3.75 \times 10^{-5}$
Direct energy gap (eV)	3.40
Optical phonon energy (meV)	72.0

### 4.3 GaN bulk results

The ionized impurity contribution to the low-field electron drift mobility for the case of GaN is shown as a function of the crystal temperature in Figure 4.1. Three cases are considered for the purposes of this particular analysis; (1) the case of  $N_T$  set to  $10^{16} \text{ cm}^{-3}$ , (2) the case of  $N_T$  set to  $10^{17} \text{ cm}^{-3}$ , and (3) the case of  $N_T$  set to  $10^{18} \text{ cm}^{-3}$ ,  $N_T$  denoting the bulk ionized impurity concentration. In keeping with the general principle of bulk charge neutrality, the electron concentration,  $n$ , is set to the bulk ionized

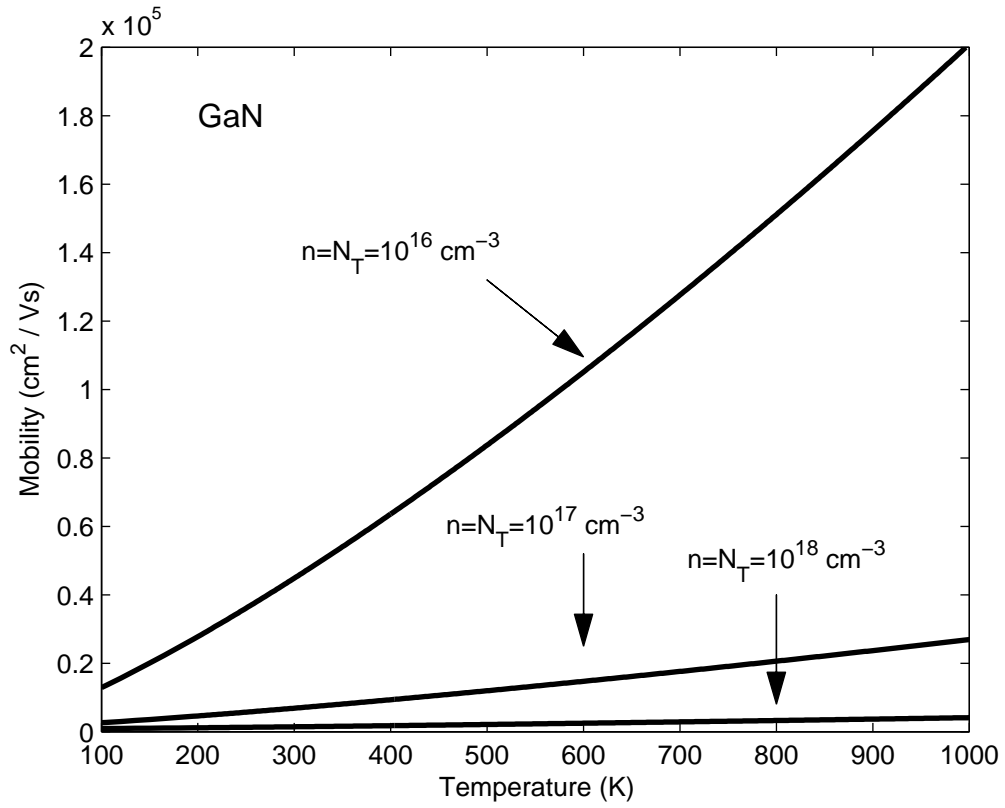


Figure 4.1: The ionized impurity contribution to the low-field electron drift mobility as a function of the crystal temperature for the case GaN. For all cases, the electron concentration,  $n$ , is set to the bulk ionized impurity concentration,  $N_T$ .

impurity concentration,  $N_T$ , for all cases. It is seen that this contribution to the electron drift monotonically increases with the crystal temperature for all cases. This monotonic dependence occurs as the thermal velocity increases monotonically with the crystal temperature, and therefore, the interaction time with the ionized impurities is reduced with greater crystal temperatures. For a fixed crystal temperature, the electron drift mobility is seen to monotonically increase with a reduction in the ionized impurity concentration. This dependence arises as a consequence of the increased ionized impurity scattering that occurs at higher ionized impurity concentrations.

Polar optical phonon scattering is an important scattering mechanism that often plays a dominant role in shaping the electron transport properties that occur within compound semiconductors and their elemental counterparts. In Figure 4.2, the contribution to the low-field electron drift mobility associated with polar optical phonon scattering is plotted as a function of the crystal temperature for the case of GaN. It is seen that this contribution to the low-field electron drift mobility diminishes with increases in the crystal temperature. Greater crystal temperatures correspond to greater numbers of polar optical phonons. This results in the observed decrease in the low-field electron drift mobility corresponding to increases in the crystal temperature.

In Figure 4.3, the contribution to the low-field electron drift mobility associated with piezoelectric scattering is plotted as a function of the crystal temperature for various selections of the electron concentration for the case of GaN. As with the polar optical phonon case, it is seen that this contribution to the low-field electron drift mobility monotonically decreases with

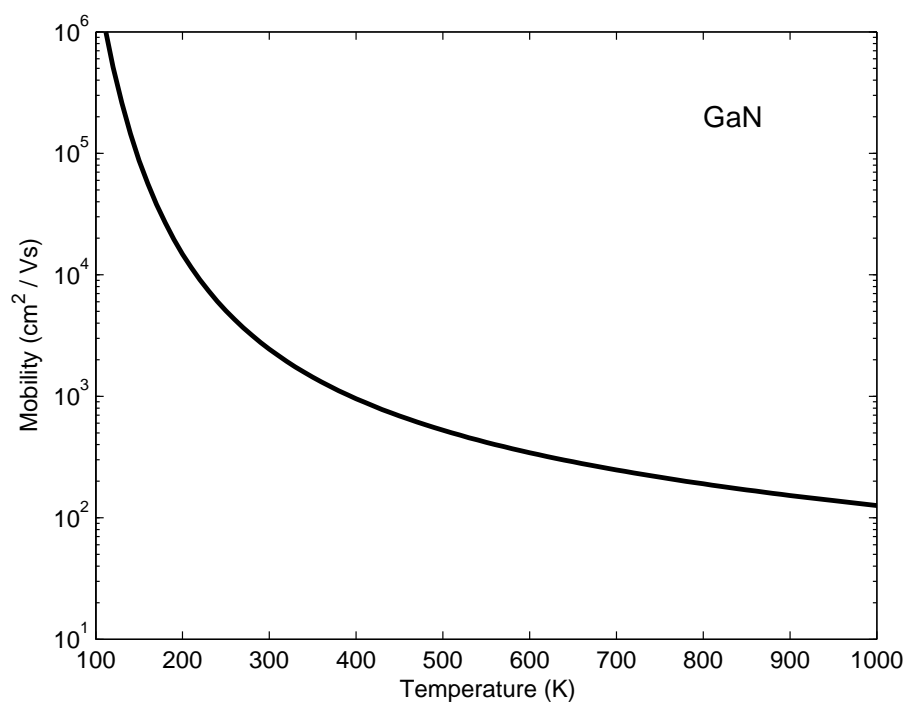


Figure 4.2: The polar optical phonon contribution to the low-field electron drift mobility as a function of the crystal temperature for the case of GaN.

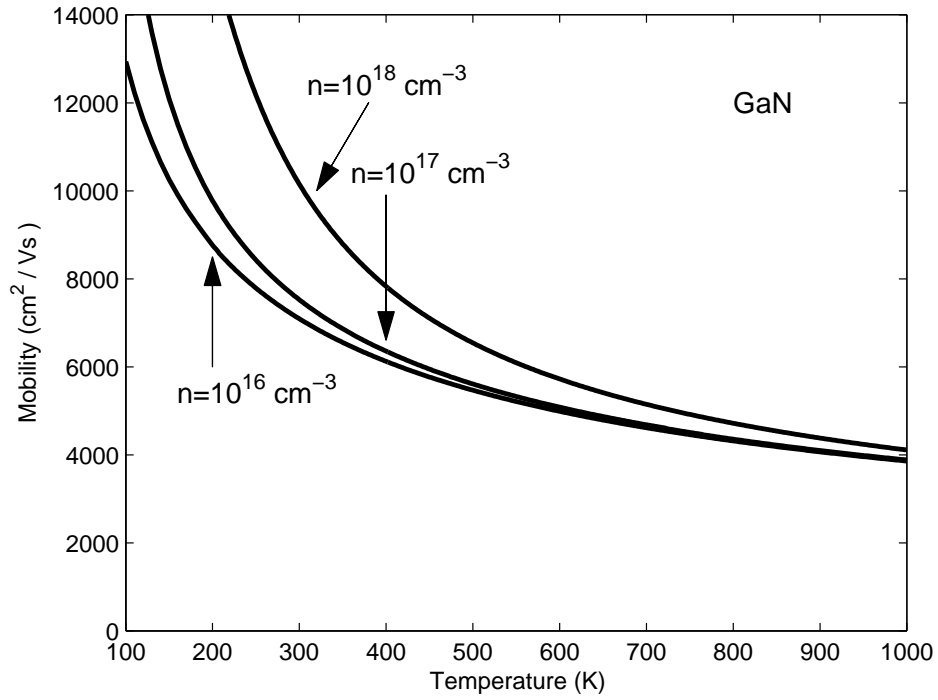


Figure 4.3: The piezoelectric contribution to the low-field electron drift mobility as a function of the crystal temperature for various selections of the electron concentration for the case of GaN.

increases in the crystal temperature. For a fixed crystal temperature, it is seen that the contribution to the low-field electron drift mobility increases monotonically with increases in the electron concentration. This trend occurs as increases in the electron concentration enhance the screening, thereby diminishing the strength of the piezoelectric scattering that occurs.

In Figure 4.4, the contribution to the low-field electron drift mobility associated with acoustic phonon deformation potential scattering is plotted as a function of the crystal temperature for the case of GaN. It is seen that this contribution to the low-field electron drift mobility monotonically decreases with increases in the crystal temperature. Greater crystal temperatures correspond to a larger number of acoustic deformation potential phonons, i.e., lattice position fluctuations of greater intensity. This results in the observed decrease in the low-field electron drift mobility.

In Figure 4.5, the contributions to the low-field electron drift mobility associated with the polar optical phonon, the piezoelectric, and the acoustic deformation potential scattering mechanisms are plotted as a function of the crystal temperature for the case of GaN. Using Eq. (3.10), the resultant combined low-field electron drift mobility is also plotted as function of the crystal temperature. For the purposes of this analysis, ionized impurity scattering is neglected, i.e., its contribution to the low-field electron drift mobility is set to infinity. The electron concentration,  $n$ , is set to  $10^{17} \text{ cm}^{-3}$  for all cases. It is seen that the combined low-field electron drift mobility monotonically decreases with increases in the crystal temperature; all of these contributions to the low-field electron drift mobility exhibit the same trend in terms of their dependence on the crystal temperature. The

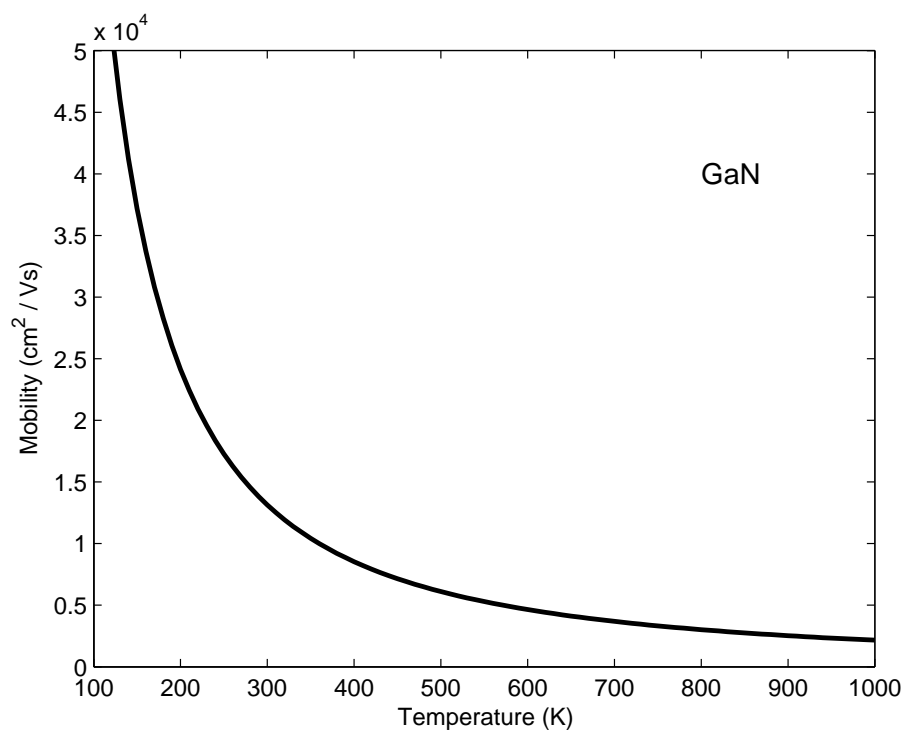


Figure 4.4: The acoustic deformation potential contribution to the low-field electron drift mobility as a function of the crystal temperature for the case of GaN.

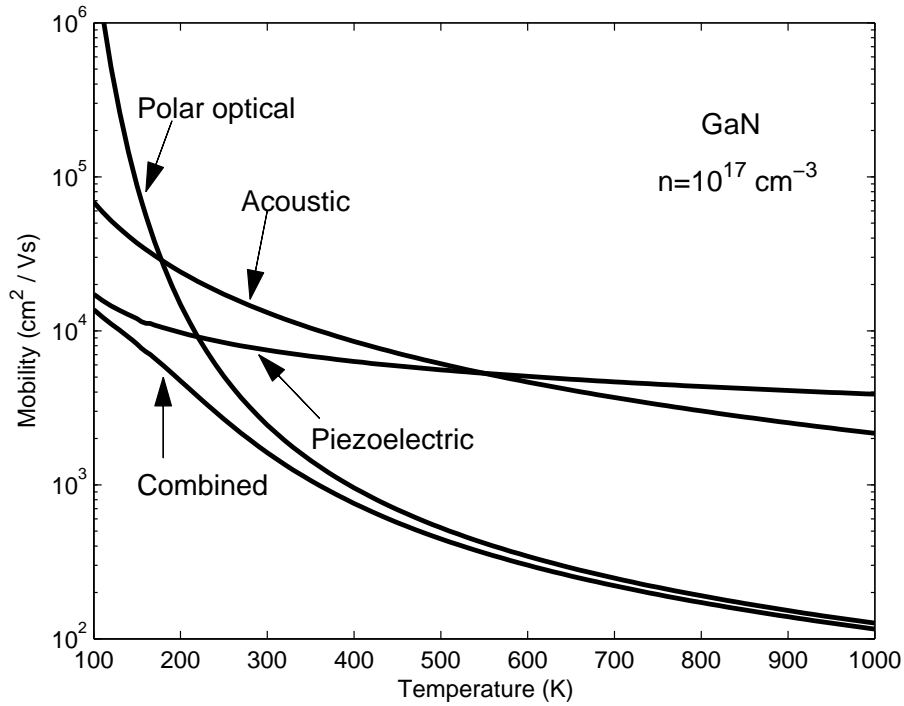


Figure 4.5: The polar optical phonon, piezoelectric, and acoustic deformation potential contributions to the low-field electron drift mobility, and the combined low-field electron drift mobility, plotted as functions of the crystal temperature for the case of GaN. For the purposes of this analysis, the ionized impurity contribution is neglected, i.e., it is set to infinity. The electron concentration,  $n$ , is set to  $10^{17} \text{ cm}^{-3}$  for all cases.

dependence of the combined low-field electron drift mobility on the crystal temperature, for various electron concentration selections, is presented in Figure 4.6, the ionized impurity contribution to the low-field electron drift mobility being neglected, as with Figure 4.5.

With ionized impurity scattering introduced, the combined low-field electron drift mobility exhibits a very different dependence on the crystal temperature for the case of GaN, as is seen in Figure 4.7. For the purposes of this analysis, the bulk ionized impurity concentration,  $N_T$ , is set to  $10^{17} \text{ cm}^{-3}$ . As the contribution to the low-field electron drift mobility associated with ionized impurity scattering monotonically increases with the crystal temperature, and the other contributions to the low-field electron drift mobility exhibit a contrary functional dependence, it should come as no surprise that at low crystal temperatures the low-field electron drift mobility exhibits a dependence that is dominated by ionized impurity scattering while at high crystal temperatures, a dependence that is dominated by the polar optical phonon, piezoelectric, and acoustic deformation potential scattering mechanisms occurs. In Figure 4.8, the combined low-field electron drift mobility is depicted for various electron and ionized impurity concentrations as a function of the crystal temperature. For all cases, the electron concentration,  $n$ , is set to the bulk ionized impurity concentration,  $N_T$ .

## 4.4 AlN bulk results

The ionized impurity contribution to the low-field electron drift mobility for the case of AlN is shown as a function of the crystal temperature

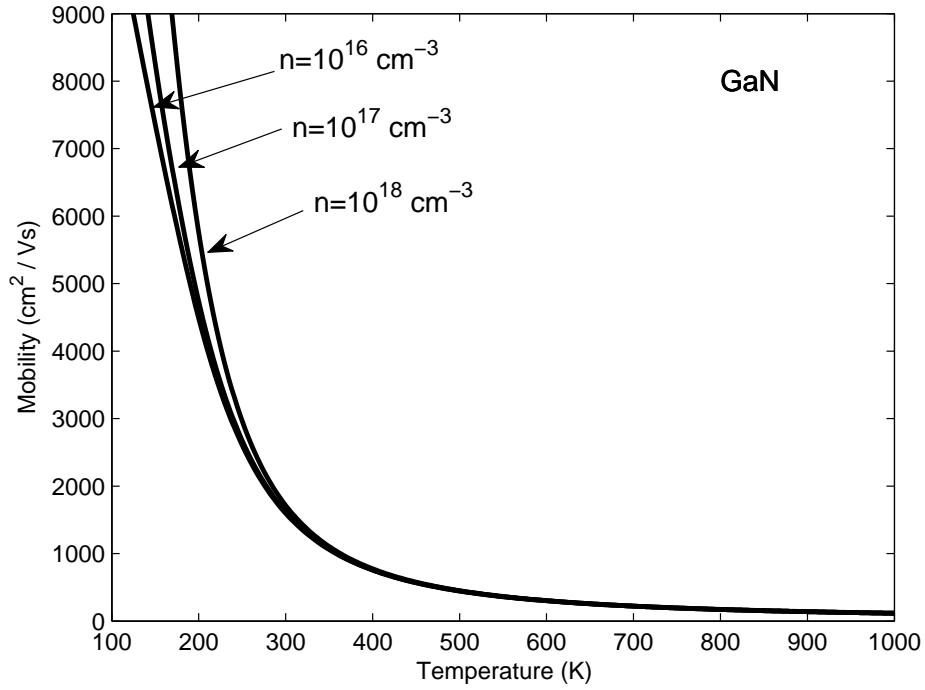


Figure 4.6: The combined low-field electron drift mobility as a function of the crystal temperature with the polar optical phonon, piezoelectric, and acoustic deformation potential scattering mechanisms taken into account for various electron concentrations for the case of GaN. For all cases, the ionized impurity contribution is neglected, i.e., it is set to infinity.

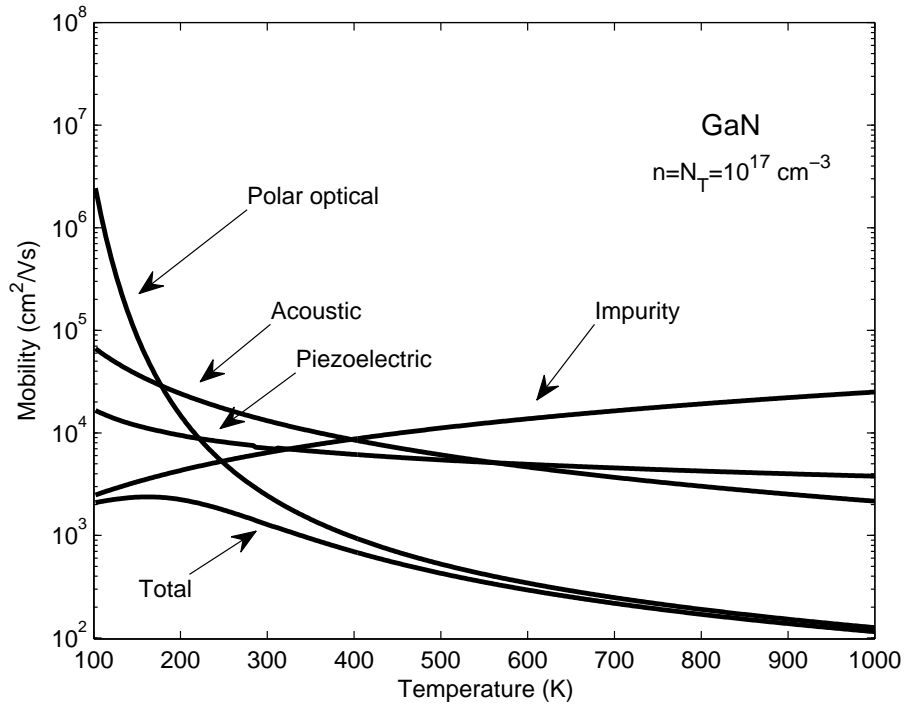


Figure 4.7: The ionized impurity, polar optical phonon, piezoelectric, and acoustic deformation potential contributions to the low-field electron drift mobility as a function of the crystal temperature for the case of GaN. The bulk ionized impurity concentration,  $N_T$ , is set to  $10^{17} \text{ cm}^{-3}$ . The electron concentration,  $n$ , is set to the bulk ionized impurity concentration,  $N_T$ .

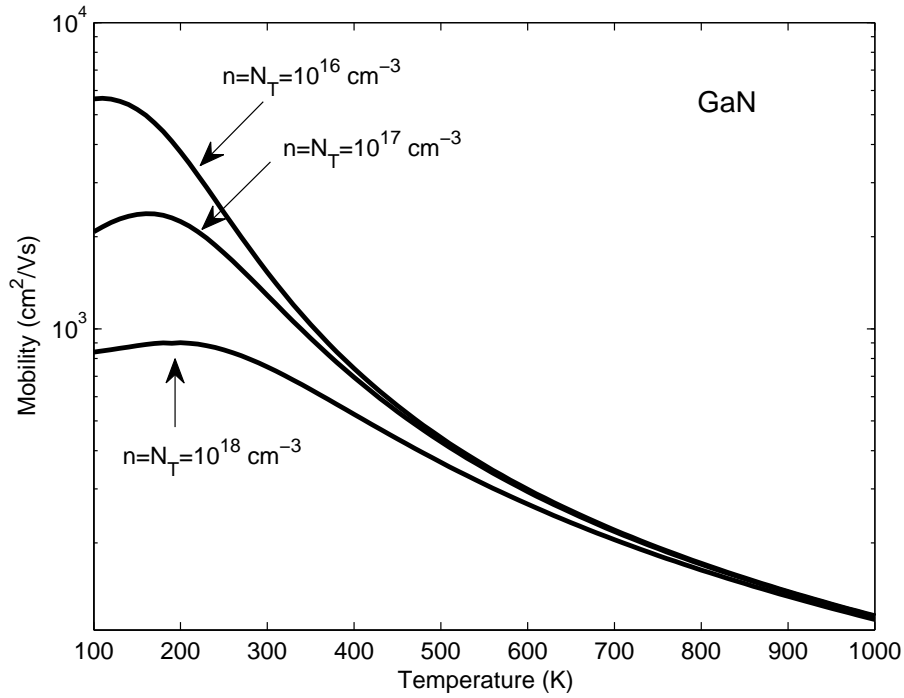


Figure 4.8: The combined low-field electron drift mobility as a function of the crystal temperature for the case of GaN. The contributions to the low-field electron drift mobility considered include those related to the ionized impurity, polar optical phonon, piezoelectric, and acoustic deformation potential scattering mechanisms. For all cases, the electron concentration,  $n$ , is set to the bulk ionized impurity concentration,  $N_T$ .

in Figure 4.9. Three cases are considered for the purposes of this particular analysis; (1) the case of  $N_T$  set to  $10^{16} \text{ cm}^{-3}$ , (2) the case of  $N_T$  set to  $10^{17} \text{ cm}^{-3}$ , and (3) the case of  $N_T$  set to  $10^{18} \text{ cm}^{-3}$ ,  $N_T$  denoting the bulk ionized impurity concentration. In keeping with the general principle of bulk charge neutrality, the electron concentration,  $n$ , is set to the bulk ionized impurity concentration,  $N_T$ , for all cases. It is seen that this contribution to the low-field electron drift mobility monotonically increases with the crystal temperature for all cases, as was observed for the case of GaN; recall Figure 4.1. This monotonic dependence occurs as the thermal velocity increases monotonically with the crystal temperature, and therefore, the interaction time with the ionized impurities is reduced with greater crystal temperatures. For a fixed crystal temperature, the low-field electron drift mobility is seen to monotonically increase with a reduction in the ionized impurity concentration. This dependence arises as a consequence of the increased ionized impurity scattering that occurs at higher ionized impurity concentrations.

In Figure 4.10, the contribution to the low-field electron drift mobility associated with polar optical phonon scattering is plotted as a function of the crystal temperature for the case of AlN. It is seen that this contribution to the low-field electron drift mobility diminishes with increases in the crystal temperature, as was observed for the case of GaN; recall Figure 4.2. Greater crystal temperatures correspond to greater numbers of polar optical phonons. This results in the observed decrease in the low-field electron drift mobility corresponding to increases in the crystal temperature.

In Figure 4.11, the contribution to the low-field electron drift mobility

#### 4.4. AlN bulk results

---

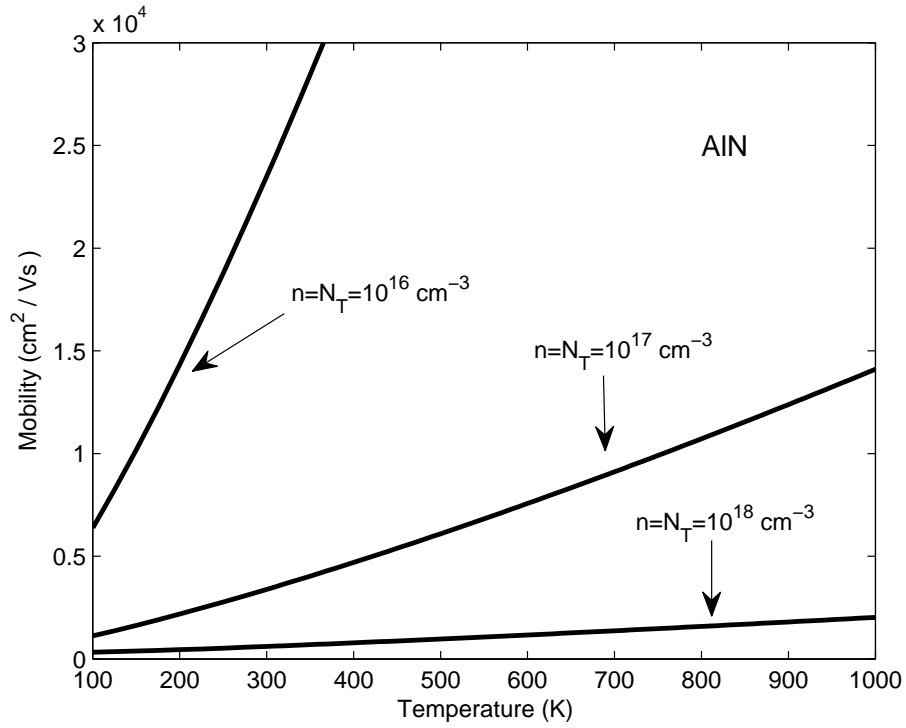


Figure 4.9: The ionized impurity contribution to the low-field electron drift mobility as a function of the crystal temperature for the case AlN. For all cases, the electron concentration,  $n$ , is set to the bulk ionized impurity concentration,  $N_T$ .

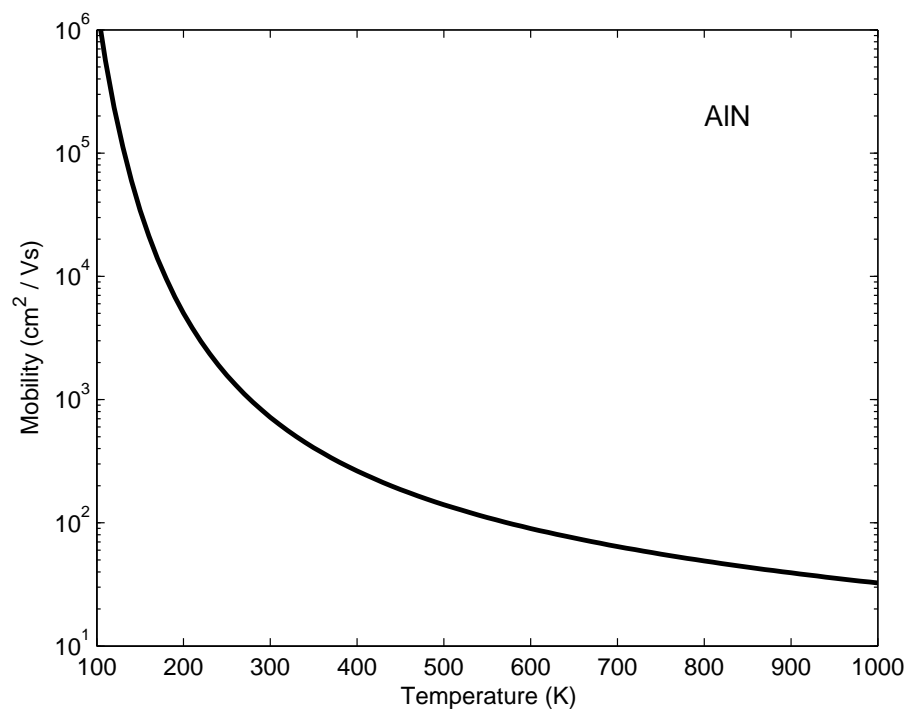


Figure 4.10: The polar optical phonon contribution to the low-field electron drift mobility as a function of the crystal temperature for the case of AlN.

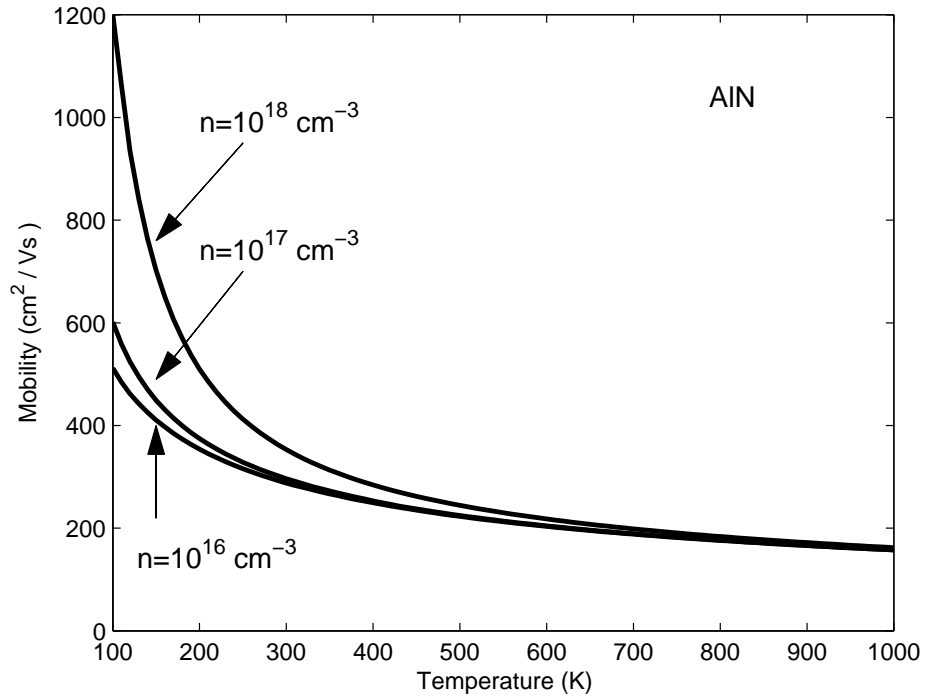


Figure 4.11: The piezoelectric contribution to the low-field electron drift mobility as a function of the crystal temperature for various selections of the electron concentration for the case of AlN.

associated with piezoelectric scattering is plotted as a function of the crystal temperature for various selections of the electron concentration for the case of AlN. As with the polar optical phonon case, it is seen that this contribution to the low-field electron drift mobility monotonically decreases with increases in the crystal temperature, as was observed for the case of GaN; recall Figure 4.3. For a fixed crystal temperature, it is seen that the contribution to the low-field electron drift mobility increases monotonically with increases in the electron concentration. This trend occurs as increases in the electron concentration enhance the screening, thereby diminishing the strength of the piezoelectric scattering that occurs.

In Figure 4.12, the contribution to the low-field electron drift mobility associated with acoustic phonon deformation potential scattering is plotted as a function of the crystal temperature for the case of AlN. It is seen that this contribution to the low-field electron drift mobility monotonically decreases with increases in the crystal temperature, as was observed for the case of GaN; recall Figure 4.4. Greater crystal temperatures correspond to a larger number of acoustic deformation potential phonons, i.e., lattice position fluctuations of greater intensity. This results in the observed decrease in the low-field electron drift mobility.

In Figure 4.13, the contributions to the low-field electron drift mobility associated with the polar optical phonon, the piezoelectric, and the acoustic deformation potential scattering mechanisms are plotted as a function of the crystal temperature for the case of AlN. Using Eq. (3.10), the resultant combined low-field electron drift mobility is also plotted as function of the crystal temperature. For the purposes of this analysis, ionized impurity

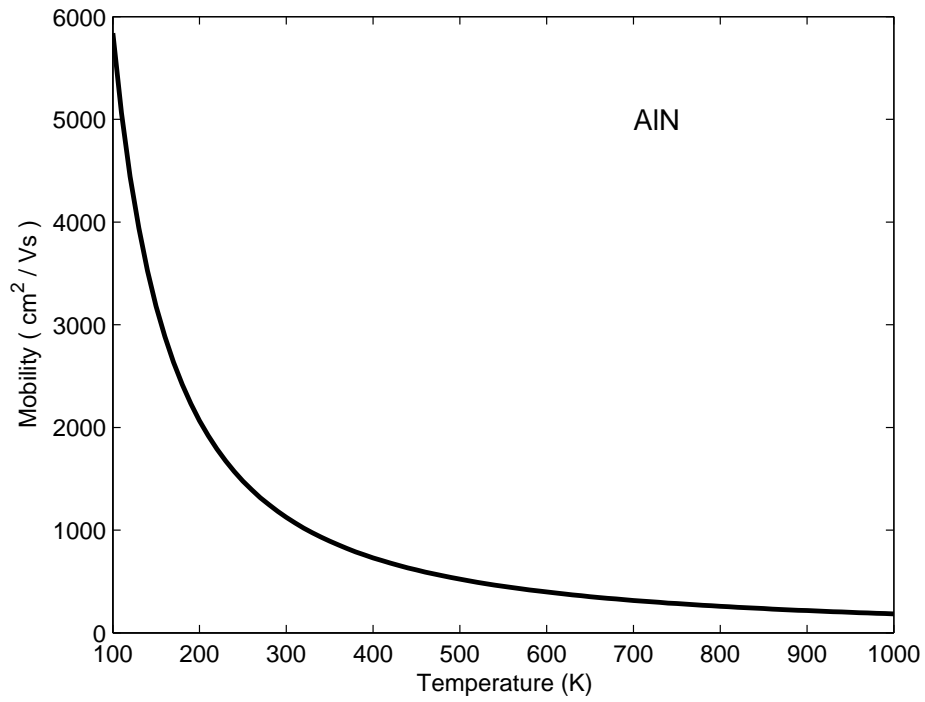


Figure 4.12: The acoustic deformation potential contribution to the low-field electron drift mobility as a function of the crystal temperature for the case of AlN.

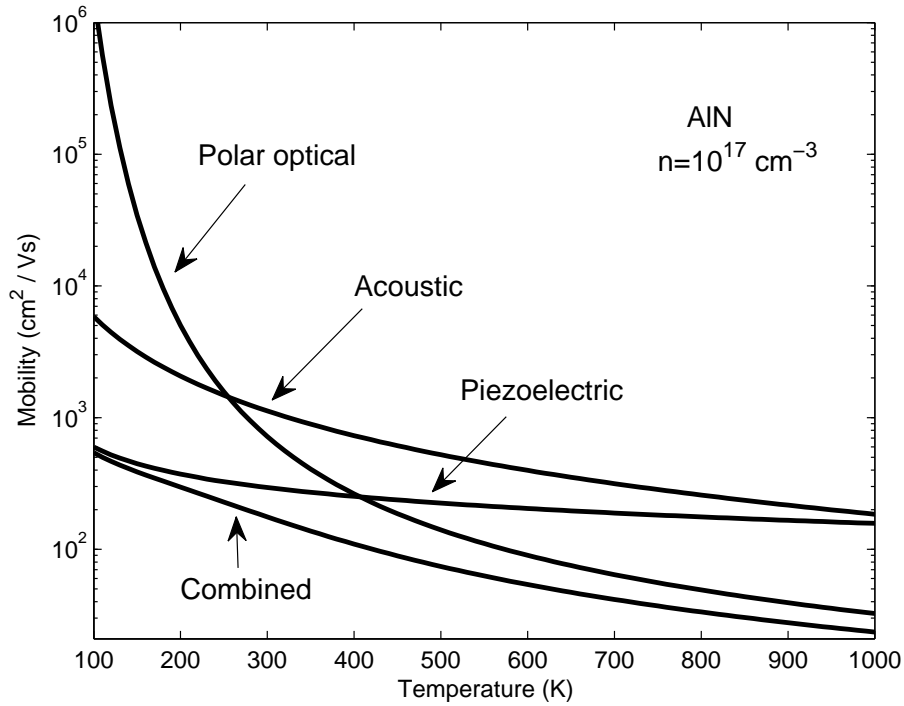


Figure 4.13: The polar optical phonon, piezoelectric, and acoustic deformation potential contributions to the low-field electron drift mobility, and the combined low-field electron drift mobility, plotted as functions of the crystal temperature for the case of AlN. For the purposes of this analysis, the ionized impurity contribution is neglected, i.e., it is set to infinity. The electron concentration,  $n$ , is set to  $10^{17} \text{ cm}^{-3}$  for all cases.

scattering is neglected, i.e., its contribution to the low-field electron drift mobility is set to infinity. The electron concentration,  $n$ , is set to  $10^{17} \text{ cm}^{-3}$  for all cases. It is seen that the combined low-field electron drift mobility monotonically decreases with increases in the crystal temperature, as was observed for the case of GaN; recall Figure 4.5; all of these contributions to the low-field electron drift mobility exhibit the same trend in terms of their dependence on the crystal temperature. The dependence of the combined low-field electron drift mobility on the crystal temperature, for various electron concentration selections, is presented in Figure 4.14, the ionized impurity contribution to the low-field electron drift mobility being neglected, as with Figure 4.13.

With ionized impurity scattering introduced, the combined low-field electron drift mobility exhibits a very different dependence on the crystal temperature for the case of AlN, as is seen in Figure 4.15. For the purposes of this analysis, the bulk ionized impurity concentration,  $N_T$ , is set to  $10^{17} \text{ cm}^{-3}$ . As the contribution to the low-field electron drift mobility associated with ionized impurity scattering monotonically increases with the crystal temperature, and the other contributions to the low-field electron drift mobility exhibit a contrary functional dependence, it should come as no surprise that at low crystal temperatures the low-field electron drift mobility exhibits a dependence that is dominated by ionized impurity scattering while at high crystal temperatures, a dependence that is dominated by the polar optical phonon, piezoelectric, and acoustic deformation potential scattering mechanisms occurs, as was observed for the case of GaN; recall Figure 4.7. In Figure 4.16, the combined low-field electron drift mobility is

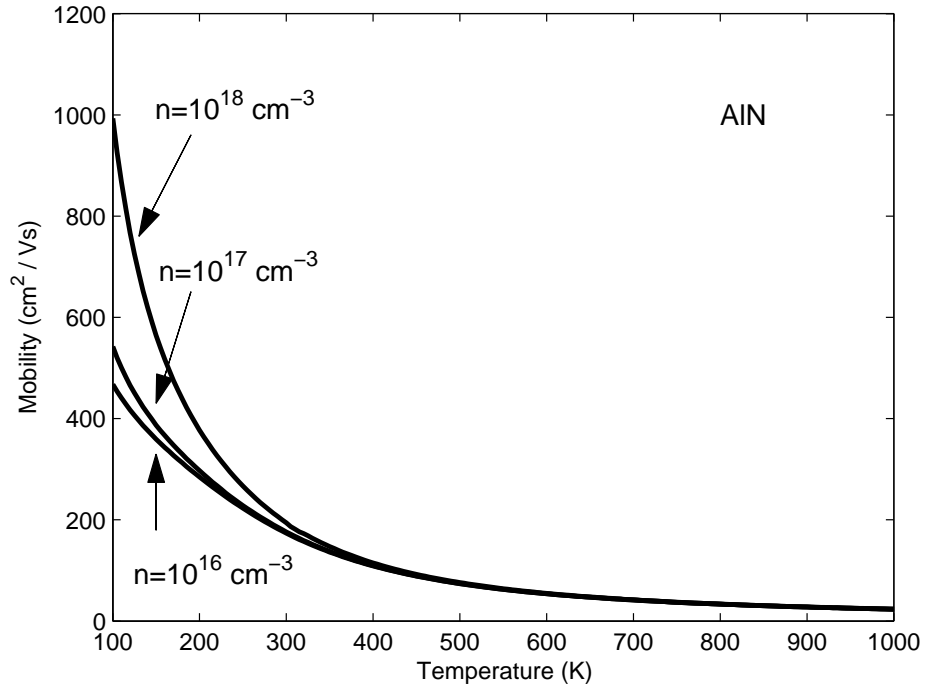


Figure 4.14: The combined low-field electron drift mobility as a function of the crystal temperature with the polar optical phonon, piezoelectric, and acoustic deformation potential scattering mechanisms taken into account for various electron concentrations for the case of AlN. For all cases, the ionized impurity contribution is neglected, i.e., it is set to infinity.

#### 4.4. AlN bulk results

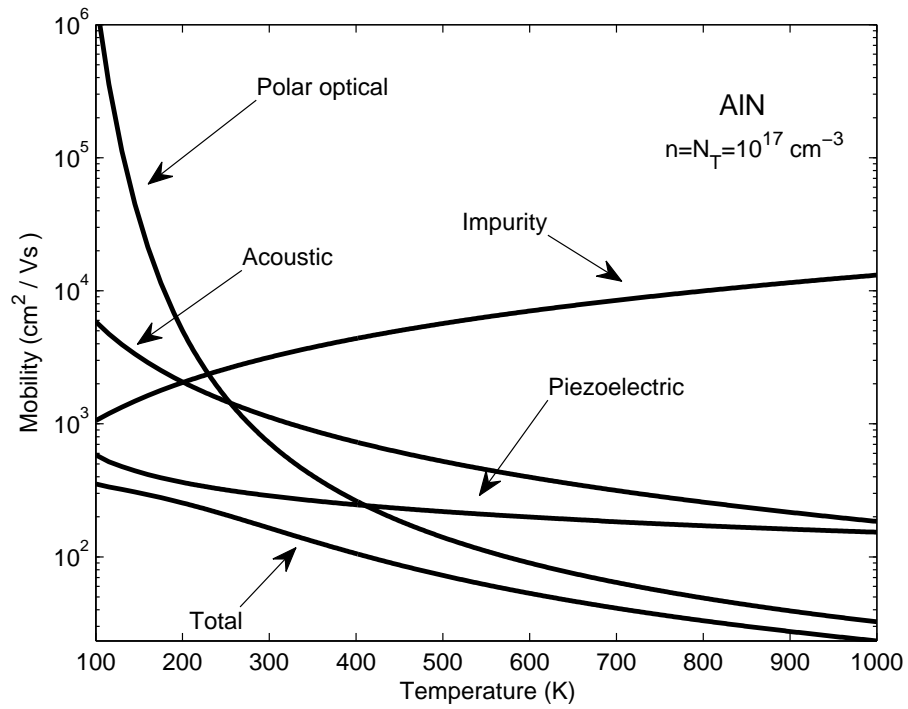


Figure 4.15: The ionized impurity, polar optical phonon, piezoelectric, and acoustic deformation potential contributions to the low-field electron drift mobility as a function of the crystal temperature for the case of AlN. The bulk ionized impurity concentration,  $N_T$ , is set to  $10^{17} \text{ cm}^{-3}$ . The electron concentration,  $n$ , is set to the bulk ionized impurity concentration,  $N_T$ .

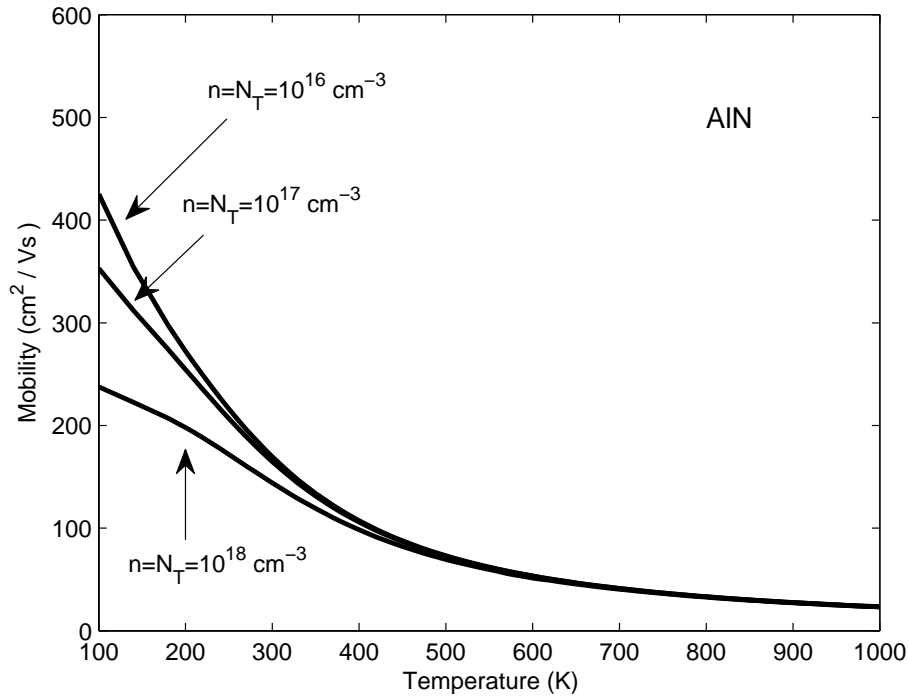


Figure 4.16: The combined low-field electron drift mobility as a function of the crystal temperature for the case of AlN. The contributions to the low-field electron drift mobility considered include those related to the ionized impurity, polar optical phonon, piezoelectric, and acoustic deformation potential scattering mechanisms. For all cases, the electron concentration,  $n$ , is set to the bulk ionized impurity concentration,  $N_T$ .

depicted for various electron and ionized impurity concentrations as a function of the crystal temperature. For all cases, the electron concentration,  $n$ , is set to the bulk ionized impurity concentration,  $N_T$ .

## 4.5 InN bulk results

The ionized impurity contribution to the low-field electron drift mobility for the case of InN is shown as a function of the crystal temperature in Figure 4.17. Three cases are considered for the purposes of this particular analysis; (1) the case of  $N_T$  set to  $10^{16} \text{ cm}^{-3}$ , (2) the case of  $N_T$  set to  $10^{17} \text{ cm}^{-3}$ , and (3) the case of  $N_T$  set to  $10^{18} \text{ cm}^{-3}$ ,  $N_T$  denoting the bulk ionized impurity concentration. In keeping with the general principle of bulk charge neutrality, the electron concentration,  $n$ , is set to the bulk ionized impurity concentration,  $N_T$ , for all cases. It is seen that this contribution to the low-field electron drift mobility monotonically increases with the crystal temperature for all cases, as was observed for the cases of GaN and AlN; recall Figures 4.1 and 4.9. This monotonic dependence occurs as the thermal velocity increases monotonically with the crystal temperature, and therefore, the interaction time with the ionized impurities is reduced with greater crystal temperatures. For a fixed crystal temperature, the low-field electron drift mobility is seen to monotonically increase with a reduction in the ionized impurity concentration. This dependence arises as a consequence of the increased ionized impurity scattering that occurs at higher ionized impurity concentrations.

In Figure 4.18, the contribution to the low-field electron drift mobility

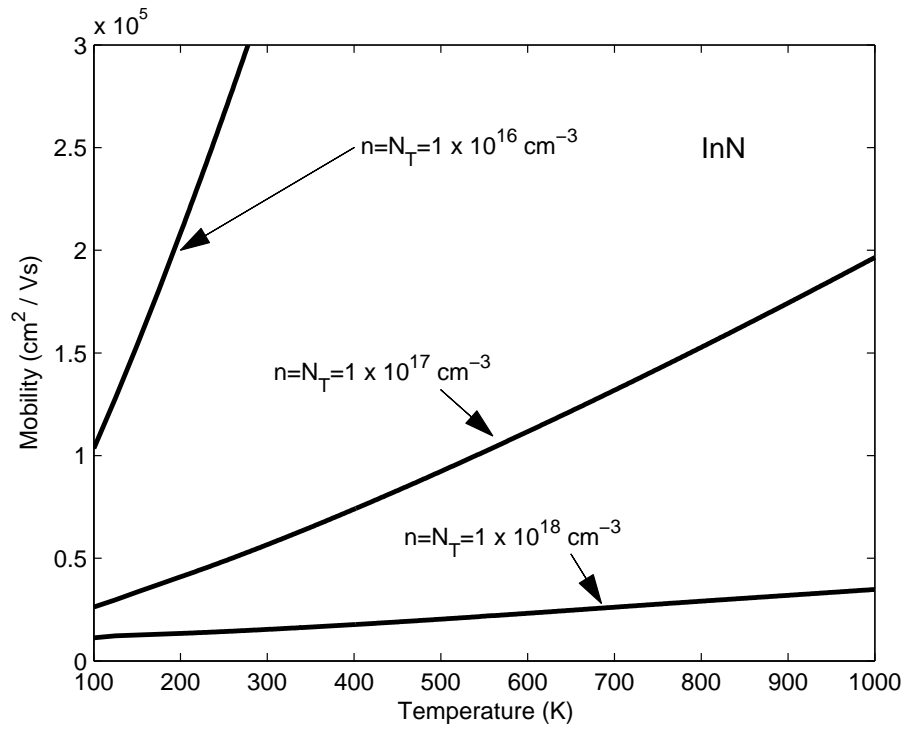


Figure 4.17: The ionized impurity contribution to the low-field electron drift mobility as a function of the crystal temperature for the case InN. For all cases, the electron concentration,  $n$ , is set to the bulk ionized impurity concentration,  $N_T$ .

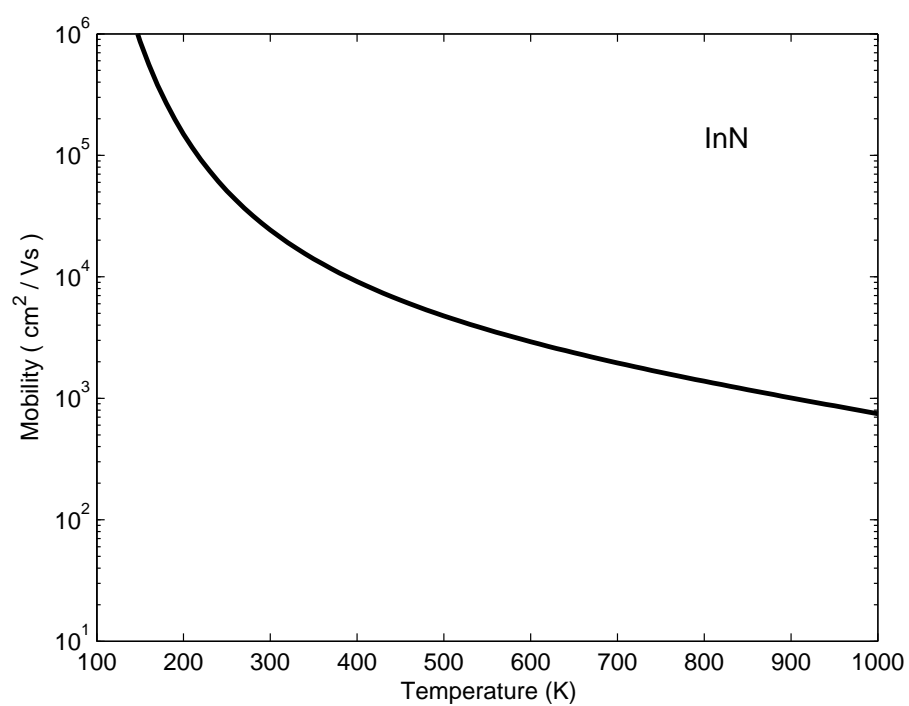


Figure 4.18: The polar optical phonon contribution to the low-field electron drift mobility as a function of the crystal temperature for the case of InN.

#### 4.5. InN bulk results

---

associated with polar optical phonon scattering is plotted as a function of the crystal temperature for the case of InN. It is seen that this contribution to the low-field electron drift mobility diminishes with increases in the crystal temperature, as was observed for the cases of GaN and AlN; recall Figures 4.2 and 4.10. Greater crystal temperatures correspond to greater numbers of polar optical phonons. This results in the observed decrease in the low-field electron drift mobility corresponding to increases in the crystal temperature.

In Figure 4.19, the contribution to the low-field electron drift mobility associated with piezoelectric scattering is plotted as a function of the crystal temperature for various selections of the electron concentration for the case of InN. In contrast to the cases of GaN and AlN, however, a distinctive non-monotonic dependence of the low-field electron drift mobility on the crystal temperature is observed for the case of the electron concentration,  $n$ , set to  $10^{18} \text{ cm}^{-3}$ . In contrast, a monotonic dependence on the crystal temperature is observed for the cases of  $n$  set to  $10^{16} \text{ cm}^{-3}$  and  $10^{17} \text{ cm}^{-3}$ , as was found for the cases of GaN and AlN; recall Figures 4.3 and 4.11. This probably arises as a consequence of the fact that the Fermi energy level is in the conduction band for this particular free electron concentration selection, i.e., the doping is degenerate. For the other cases, however, it is seen that this contribution to the low-field electron drift mobility monotonically decreases with increases in the crystal temperature.

In Figure 4.20, the contribution to the low-field electron drift mobility associated with acoustic phonon deformation potential scattering is plotted as a function of the crystal temperature for the case of InN. It is seen that this

4.5. InN bulk results

---

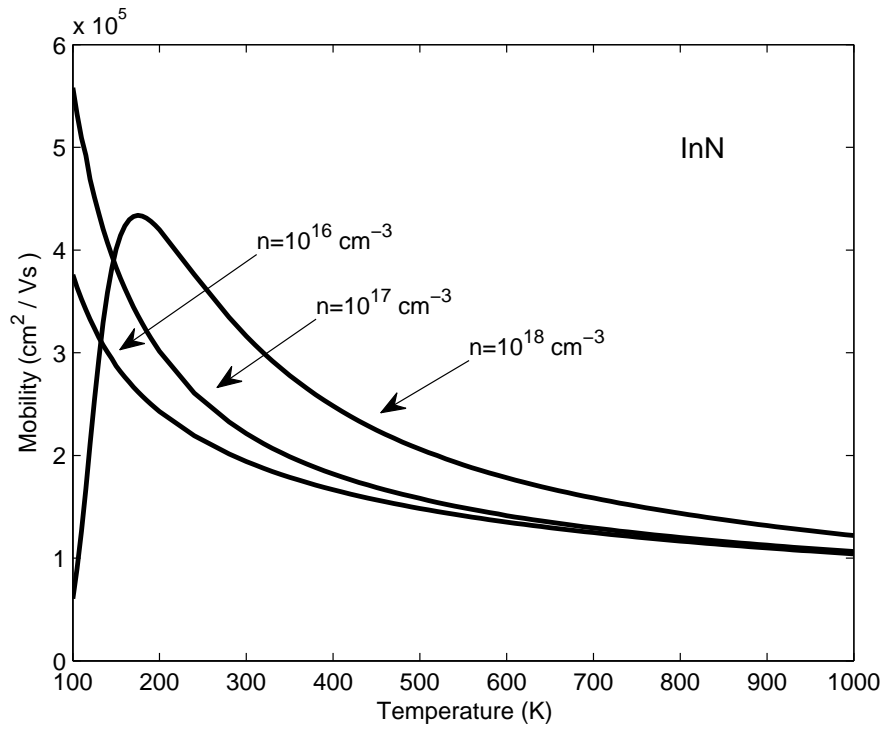


Figure 4.19: The piezoelectric contribution to the low-field electron drift mobility as a function of the crystal temperature for various selections of the electron concentration for the case of InN.

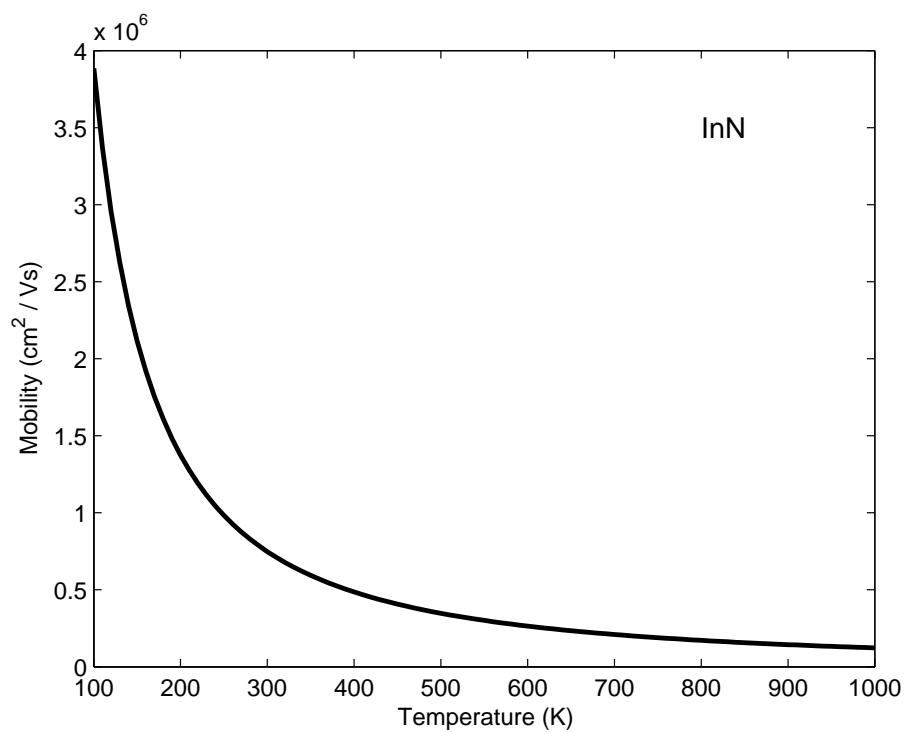


Figure 4.20: The acoustic deformation potential contribution to the low-field electron drift mobility as a function of the crystal temperature for the case of InN.

contribution to the low-field electron drift mobility monotonically decreases with increases in the crystal temperature, as was observed for the cases of GaN and AlN; recall Figures 4.4 and 4.12. Greater crystal temperatures correspond to a larger number of acoustic deformation potential phonons, i.e., lattice position fluctuations of greater intensity. This results in the observed decrease in the low-field electron drift mobility.

In Figure 4.21, the contributions to the low-field electron drift mobility associated with the polar optical phonon, the piezoelectric, and the acoustic deformation potential scattering mechanisms are plotted as a function of the crystal temperature for the case of InN. Using Eq. (3.10), the resultant combined low-field electron drift mobility is also plotted as function of the crystal temperature. For the purposes of this analysis, ionized impurity scattering is neglected, i.e., its contribution to the low-field electron drift mobility is set to infinity. The electron concentration,  $n$ , is set to  $10^{17} \text{ cm}^{-3}$  for all cases. It is seen that the combined low-field electron drift mobility monotonically decreases with increases in the crystal temperature, as was observed for the cases of GaN and AlN; recall Figures 4.5 and 4.13; all of these contributions to the low-field electron drift mobility exhibit the same trend in terms of their dependence on the crystal temperature. The dependence of the combined low-field electron drift mobility on the crystal temperature, for various electron concentration selections, is presented in Figure 4.22, the ionized impurity contribution to the low-field electron drift mobility being neglected, as with Figure 4.21.

With ionized impurity scattering introduced, the combined low-field electron drift mobility exhibits a very different dependence on the crystal tem-

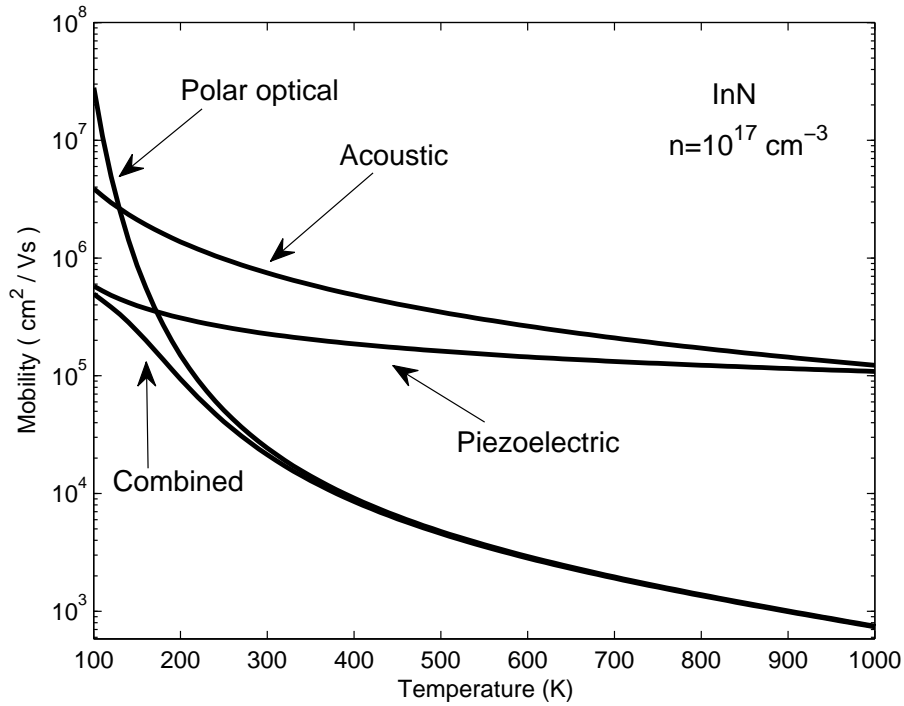


Figure 4.21: The polar optical phonon, piezoelectric, and acoustic deformation potential contributions to the low-field electron drift mobility, and the combined low-field electron drift mobility, plotted as functions of the crystal temperature for the case of InN. For the purposes of this analysis, the ionized impurity contribution is neglected, i.e., it is set to infinity. The electron concentration,  $n$ , is set to  $10^{17} \text{ cm}^{-3}$  for all cases.

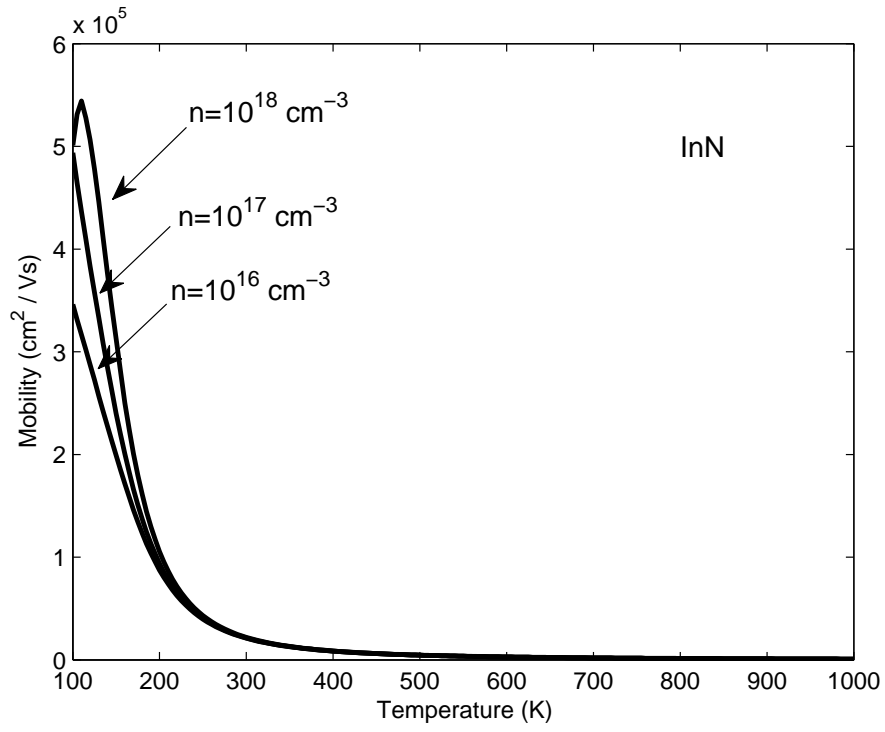


Figure 4.22: The combined low-field electron drift mobility as a function of the crystal temperature with the polar optical phonon, piezoelectric, and acoustic deformation potential scattering mechanisms taken into account for various electron concentrations for the case of InN. For all cases, the ionized impurity contribution is neglected, i.e., it is set to infinity.

perature for the case of InN, as is seen in Figure 4.23. For the purposes of this analysis, the bulk ionized impurity concentration,  $N_T$ , is set to  $10^{17} \text{ cm}^{-3}$ . As the contribution to the low-field electron drift mobility associated with ionized impurity scattering monotonically increases with the crystal temperature, and the other contributions to the low-field electron drift mobility exhibit a contrary functional dependence, it should come as no surprise that at low crystal temperatures the low-field electron drift mobility exhibits a dependence that is dominated by ionized impurity scattering while at high crystal temperatures, a dependence that is dominated by the polar optical phonon, piezoelectric, and acoustic deformation potential scattering mechanisms occurs, as was observed for the cases of GaN and AlN; recall the Figures 4.7 and 4.15. In Figure 4.24, the combined low-field electron drift mobility is depicted for various electron and ionized impurity concentrations as a function of the crystal temperature. For all cases, the electron concentration,  $n$ , is set to the bulk ionized impurity concentration,  $N_T$ .

## 4.6 ZnO bulk results

The ionized impurity contribution to the low-field electron drift mobility for the case of ZnO is shown as a function of the crystal temperature in Figure 4.25. Three cases are considered for the purposes of this particular analysis; (1) the case of  $N_T$  set to  $10^{16} \text{ cm}^{-3}$ , (2) the case of  $N_T$  set to  $10^{17} \text{ cm}^{-3}$ , and (3) the case of  $N_T$  set to  $10^{18} \text{ cm}^{-3}$ ,  $N_T$  denoting the bulk ionized impurity concentration. In keeping with general principle of bulk charge neutrality, the electron concentration,  $n$ , is set to the bulk

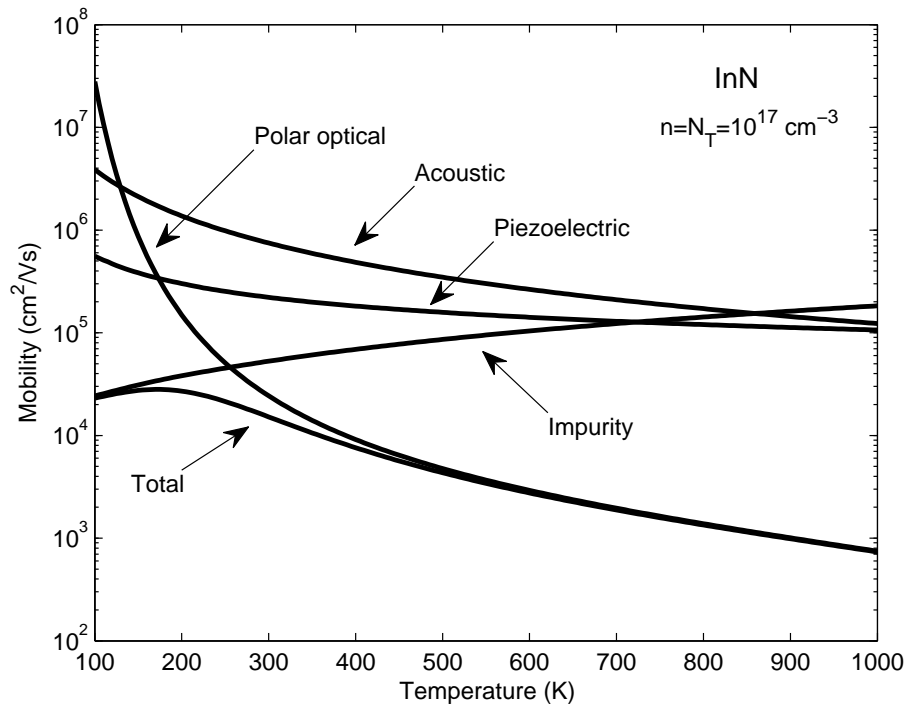


Figure 4.23: The ionized impurity, polar optical phonon, piezoelectric, and acoustic deformation potential contributions to the low-field electron drift mobility as a function of the crystal temperature for the case of InN. The bulk ionized impurity concentration,  $N_T$ , is set to  $10^{17} \text{ cm}^{-3}$ . The electron concentration,  $n$ , is set to the bulk ionized impurity concentration,  $N_T$ .

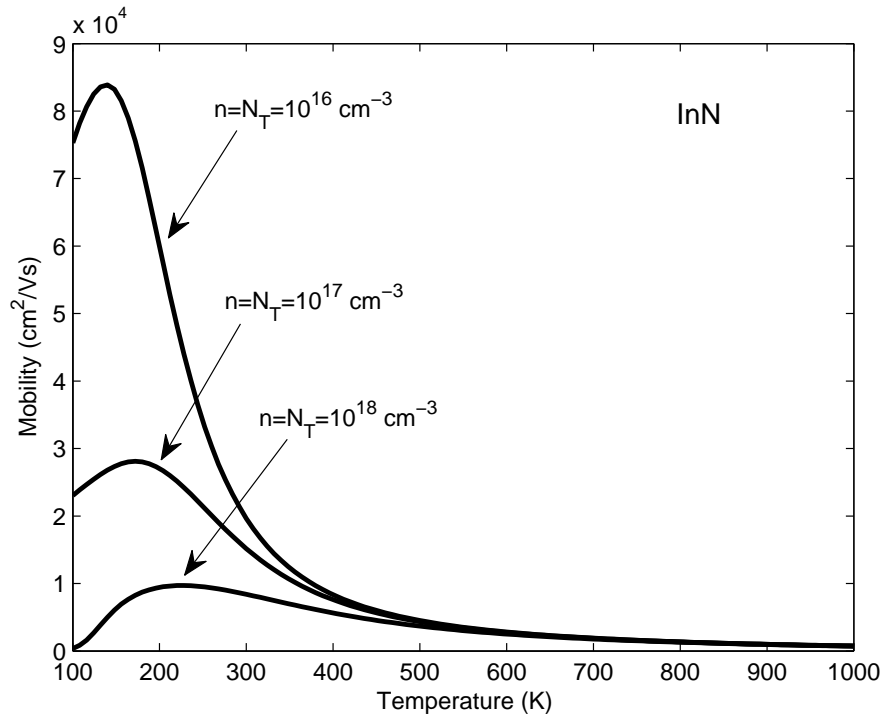


Figure 4.24: The combined low-field electron drift mobility as a function of the crystal temperature for the case of InN. The contributions to the low-field electron drift mobility considered include those related to the ionized impurity, polar optical phonon, piezoelectric, and acoustic deformation potential scattering mechanisms. For all cases, the electron concentration,  $n$ , is set to the bulk ionized impurity concentration,  $N_T$ .

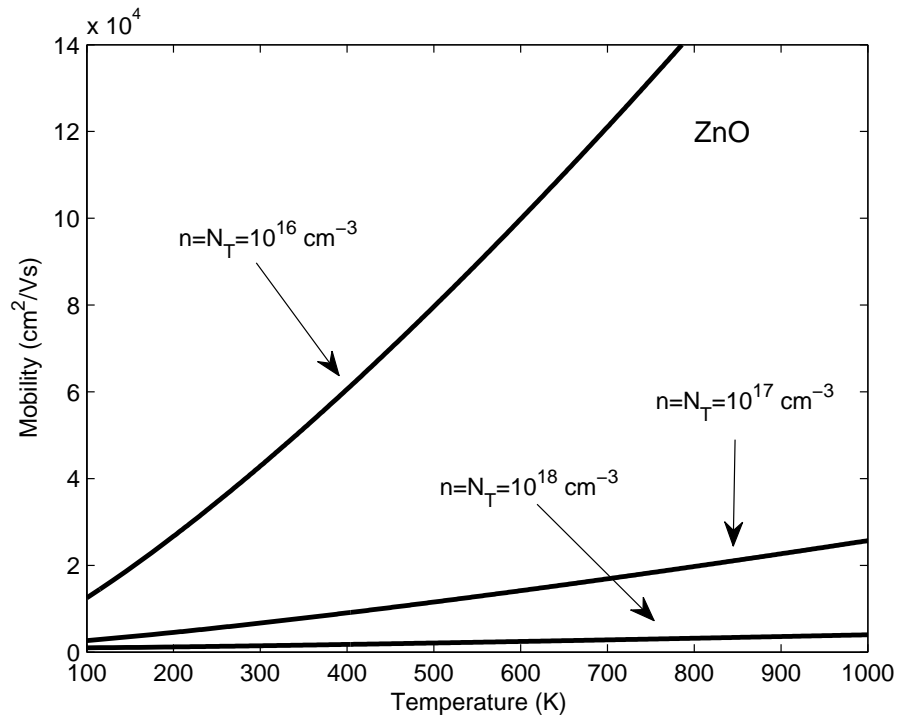


Figure 4.25: The ionized impurity contribution to the low-field electron drift mobility as a function of the crystal temperature for the case ZnO. For all cases, the electron concentration,  $n$ , is set to the bulk ionized impurity concentration,  $N_T$ .

ionized impurity concentration,  $N_T$ , for all cases. It is seen that this contribution to the low-field electron drift mobility monotonically increases with the crystal temperature for all cases, as was observed for the cases of GaN, AlN, and InN; recall Figures 4.1, 4.9, and 4.17. This monotonic dependence occurs as the thermal velocity increases monotonically with the crystal temperature, and therefore, the interaction time with the ionized impurities is reduced with greater crystal temperatures. For a fixed crystal temperature, the low-field electron drift mobility is seen to monotonically increase with a reduction in the ionized impurity concentration. This dependence arises as a consequence of the increased ionized impurity scattering that occurs at higher ionized impurity concentrations.

In Figure 4.26, the contribution to the low-field electron drift mobility associated with polar optical phonon scattering is plotted as a function of the crystal temperature for the case of ZnO. It is seen that this contribution to the low-field electron drift mobility diminishes with increases in the crystal temperature, as was observed for the cases of GaN, AlN, and InN; recall Figures 4.2, 4.10, and 4.18. Greater crystal temperatures correspond to greater numbers of polar optical phonons. This results in the observed decrease in the low-field electron drift mobility corresponding to increases in the crystal temperature.

In Figure 4.27, the contribution to the low-field electron drift mobility associated with piezoelectric scattering is plotted as a function of the crystal temperature for various selections of the electron concentration for the case of ZnO. As with the polar optical phonon case, it is seen that this contribution to the electron drift mobility monotonically decreases with increases

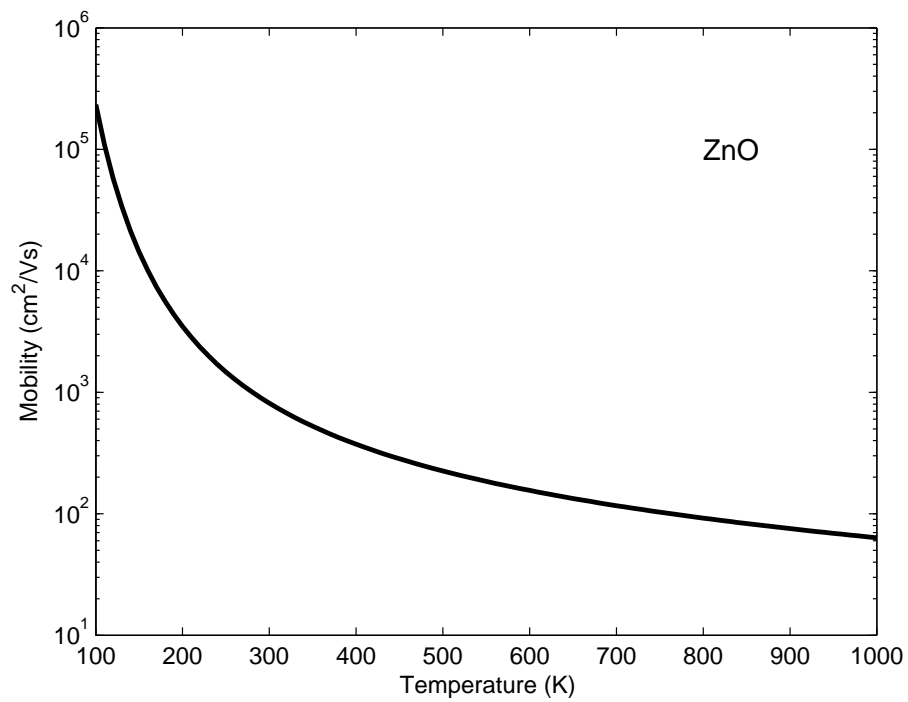


Figure 4.26: The polar optical phonon contribution to the low-field electron drift mobility as a function of the crystal temperature for the case of ZnO.

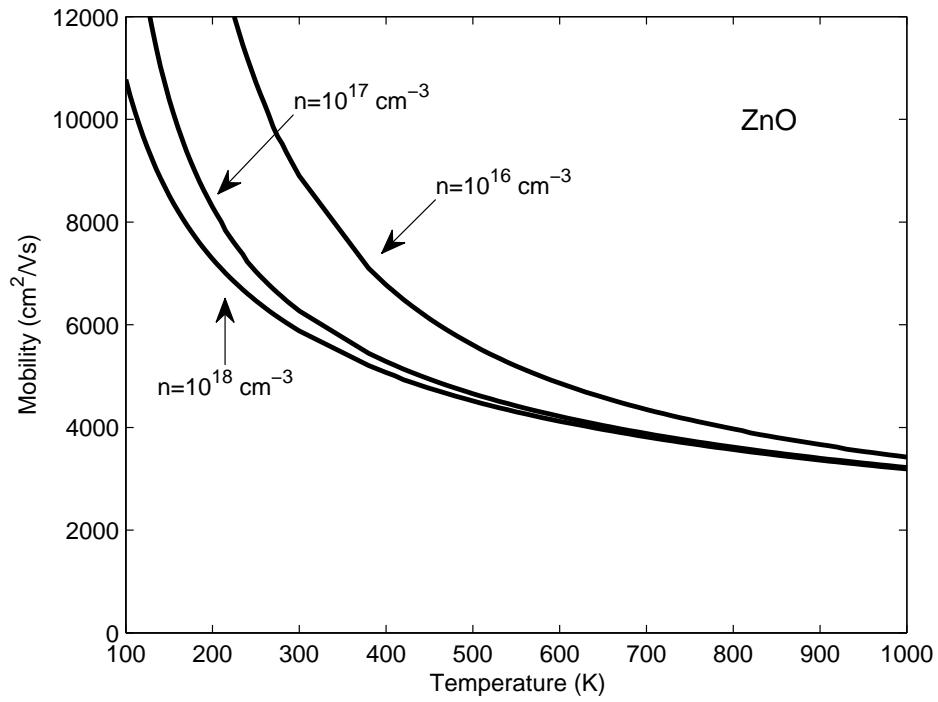


Figure 4.27: The piezoelectric contribution to the low-field electron drift mobility as a function of the crystal temperature for various selections of the electron concentration for the case of ZnO.

in the crystal temperature, as was observed for the cases of GaN, AlN, and InN for low electron concentrations; recall Figures 4.3, 4.11, and 4.15. For a fixed crystal temperature, it is seen that the contribution to the low-field electron drift mobility increases monotonically with increases in the electron concentration. This trend occurs as increases in the electron concentration enhance the screening, thereby diminishing the strength of the piezoelectric scattering that occurs.

In Figure 4.28, the contribution to the low-field electron drift mobility associated with acoustic phonon deformation potential scattering is plotted as a function of the crystal temperature for the case of ZnO. It is seen that this contribution to the low-field electron drift mobility monotonically decreases with increases in the crystal temperature, as was observed for the cases of GaN, AlN, and InN; recall Figures 4.4, 4.12, and 4.20. Greater crystal temperatures correspond to a larger number of acoustic deformation potential phonons, i.e., lattice position fluctuations of greater intensity. This results in the observed decrease in the low-field electron drift mobility.

In Figure 4.29, the contributions to the low-field electron drift mobility associated with the polar optical phonon, the piezoelectric, and the acoustic deformation potential scattering mechanisms are plotted as a function of the crystal temperature for the case of ZnO. Using Eq. (3.10), the resultant combined low-field electron drift mobility is plotted as function of the crystal temperature. For the purposes of this analysis, ionized impurity scattering is neglected, i.e., its contribution to the low-field electron drift mobility is set to infinity. The electron concentration,  $n$ , is set to  $10^{17} \text{ cm}^{-3}$  for all cases. It is seen that the combined low-field electron drift mobility monotonically

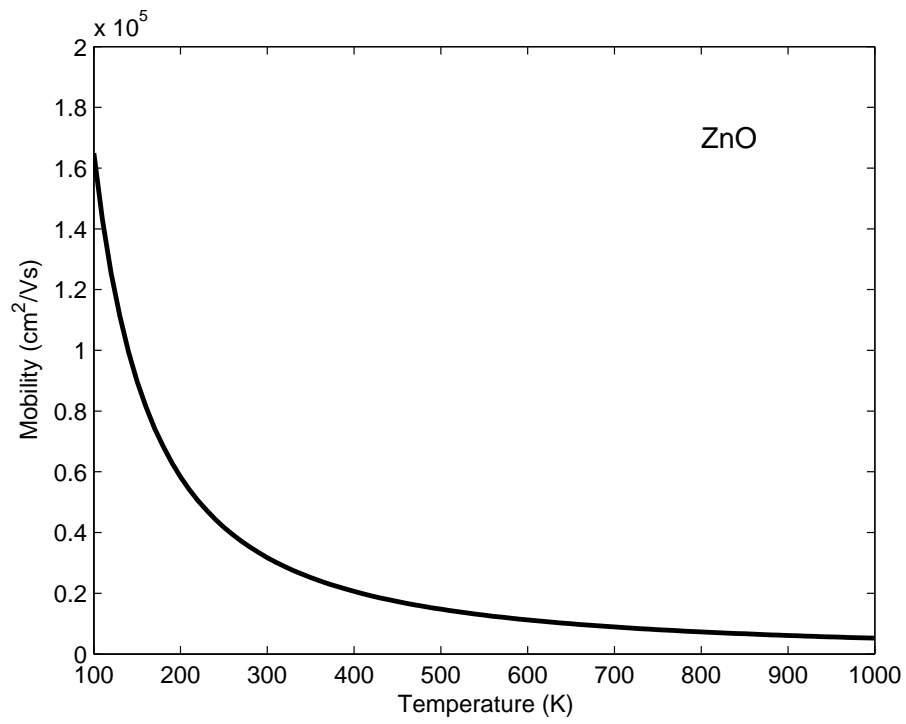


Figure 4.28: The acoustic deformation potential contribution to the low-field electron drift mobility as a function of the crystal temperature for the case of ZnO.

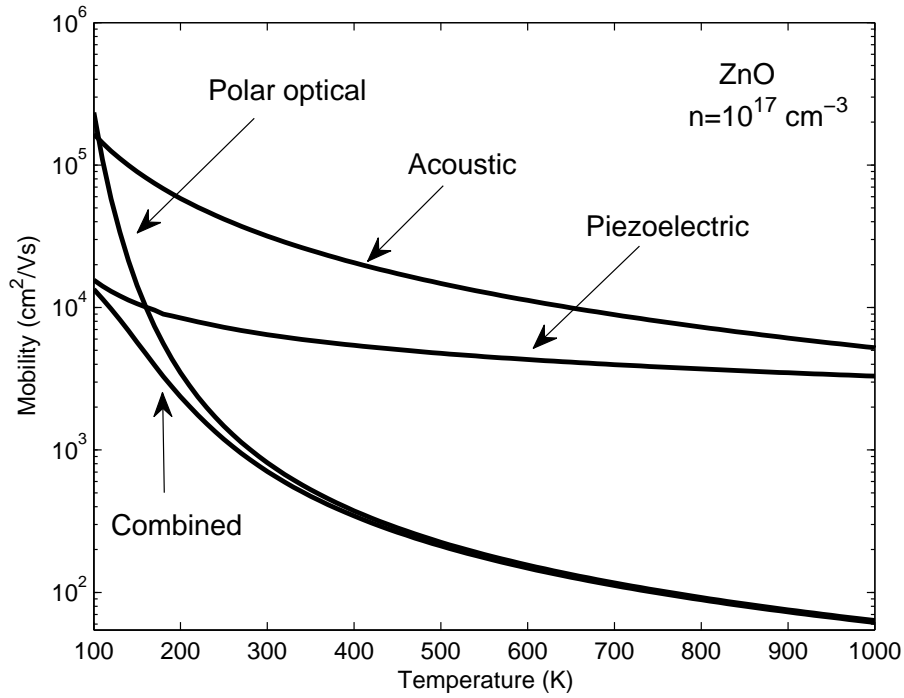


Figure 4.29: The polar optical phonon, piezoelectric, and acoustic deformation potential contributions to the low-field electron drift mobility, and the combined low-field electron drift mobility, plotted as functions of the crystal temperature for the case of ZnO. For the purposes of this analysis, the ionized impurity contribution is neglected, i.e., it is set to infinity. The electron concentration,  $n$ , is set to  $10^{17} \text{ cm}^{-3}$  for all cases.

decreases with increases in the crystal temperature, as was observed for the cases of GaN, AlN, and InN; recall Figures 4.5, 4.13, and 4.21; all of these contributions to the low-field electron drift mobility exhibit the same trend in terms of their dependence on the crystal temperature. The dependence of the combined low-field electron drift mobility on the crystal temperature, for various electron concentration selections, is presented in Figure 4.30, the ionized impurity contribution to the low-field electron drift mobility being neglected, as with Figure 4.29.

With ionized impurity scattering introduced, the combined low-field electron drift mobility exhibits a very different dependence on the crystal temperature for the case of ZnO, as is seen in Figure 4.31. For the purposes of this analysis, the bulk ionized impurity concentration,  $N_T$ , is set to  $10^{17} \text{ cm}^{-3}$ . As the contribution to the low-field electron drift mobility associated with ionized impurity scattering monotonically increases with the crystal temperature, and the other contributions to the low-field electron drift mobility exhibit a contrary functional dependence, it should come as no surprise that at low crystal temperatures the low-field electron drift mobility exhibits a dependence that is dominated by ionized impurity scattering while at high crystal temperatures, a dependence that is dominated by the polar optical phonon, piezoelectric, and acoustic deformation potential scattering mechanisms occurs, as was observed for the cases of GaN, AlN, and InN; recall the Figures 4.7, 4.15, and 4.23. In Figure 4.32, the combined low-field electron drift mobility is depicted for various electron and ionized impurity concentrations as a function of the crystal temperature. For all cases, the electron concentration,  $n$ , is set to the bulk ionized

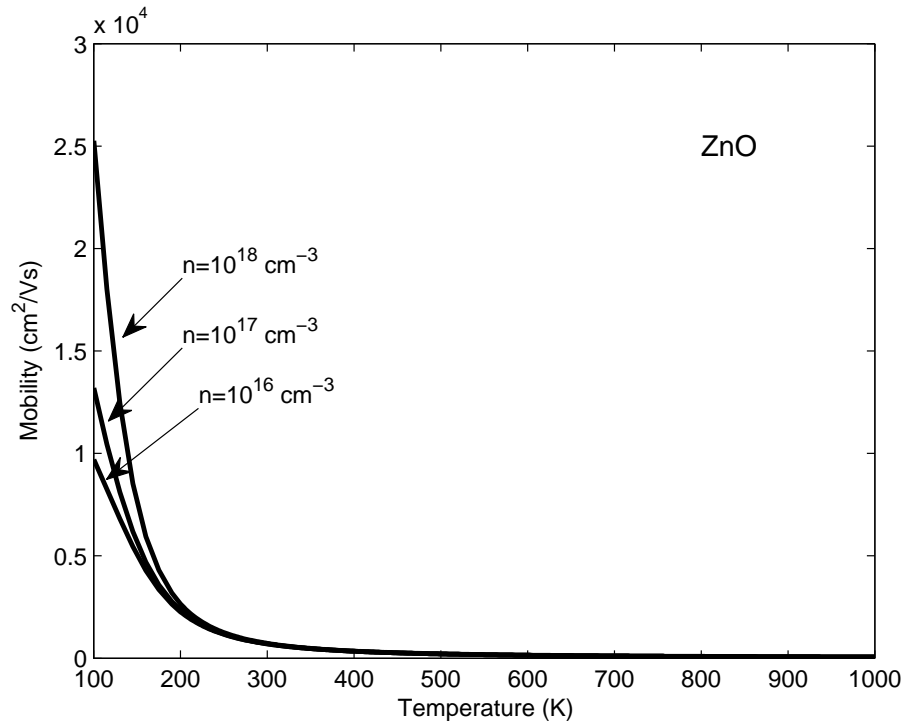


Figure 4.30: The combined low-field electron drift mobility plotted as a function of the crystal temperature with the polar optical phonon, piezoelectric, and acoustic deformation potential scattering mechanisms taken into account for various electron concentrations for the case of ZnO. For all cases, the ionized impurity contribution is neglected, i.e., it is set to infinity.

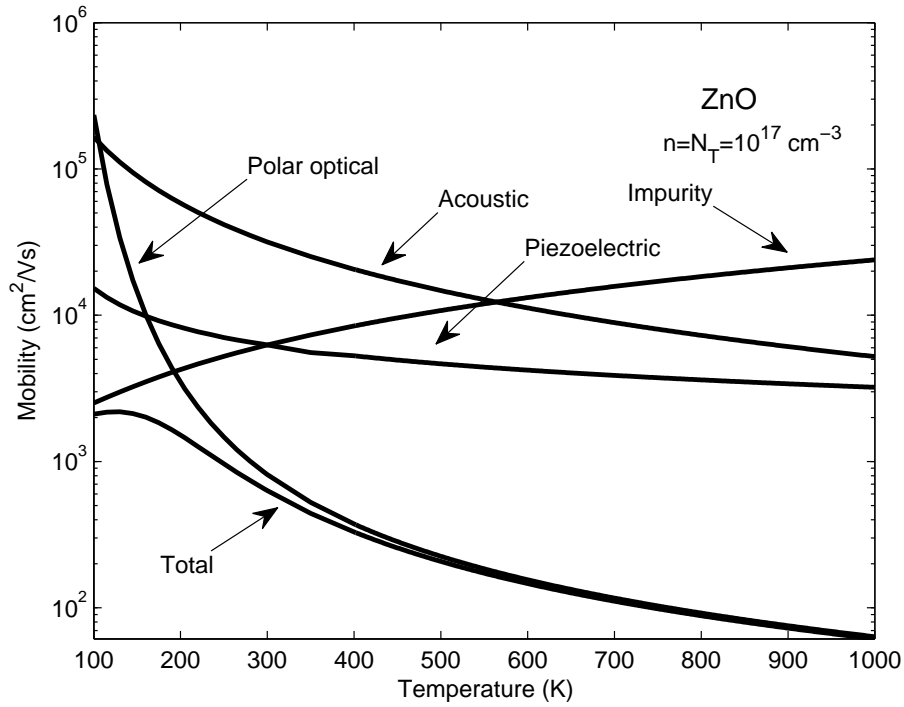


Figure 4.31: The ionized impurity, polar optical phonon, piezoelectric, and acoustic deformation potential contributions to the low-field electron drift mobility as a function of the crystal temperature for the case of ZnO. The bulk ionized impurity concentration,  $N_T$ , is set to  $10^{17} \text{ cm}^{-3}$ . The electron concentration,  $n$ , is set to the bulk ionized impurity concentration,  $N_T$ .

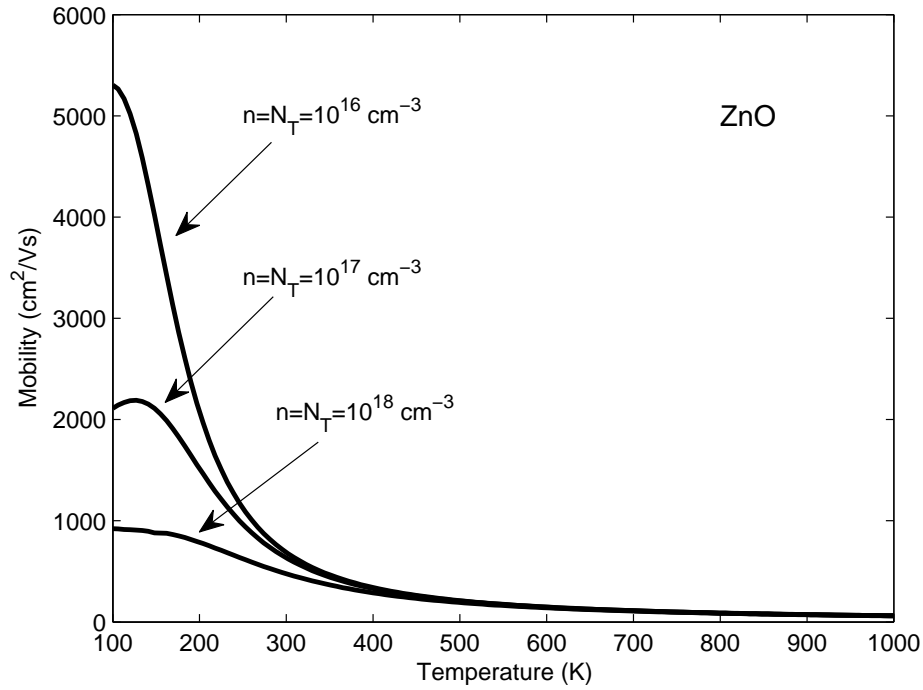


Figure 4.32: The combined low-field electron drift mobility as a function of the crystal temperature for the case of ZnO. The contributions to the low-field electron drift mobility considered include those related to the ionized impurity, polar optical phonon, piezoelectric, and acoustic deformation potential scattering mechanisms. For all cases, the electron concentration,  $n$ , is set to the bulk ionized impurity concentration,  $N_T$ .

impurity concentration,  $N_T$ .

## 4.7 A comparison of the bulk results

In Figure 4.33, the dependence of the low-field electron drift mobility on the crystal temperature is depicted for all the semiconductor materials that were considered in the analysis, i.e., GaN, AlN, InN, and ZnO. For all cases, the ionized impurity, polar optical phonon, piezoelectric, and acoustic deformation potential scattering mechanisms are included, Eq. (3.10) allowing for the determination of the combined low-field electron drift mobility. It is noted that InN exhibits the highest combined low-field electron drift mobility when compared with the other materials. This undoubtedly arises as a consequence its light conduction band effective mass; recall Figure 2.6 and Table 4.1. In contrast, AlN exhibits the lowest low-field electron drift mobility, this being due to its heavy conduction band effective mass; recall Table 4.1. ZnO and GaN exhibit a low-field electron drift mobility dependence on the crystal temperature that coincides for temperatures below 150 K, but separates for temperatures in excess of 150 K. The greater high temperature low-field electron drift mobility associated with GaN is related to the fact that its polar optical phonon energy is larger than that associated with ZnO; from Table 4.1, it is seen that the polar optical phonon energy, i.e., associated with GaN and ZnO are 91.2 and 72 meV, respectively. This implies that more thermal energy will be required to produce polar optical phonons in GaN than in ZnO. Thus, at a given temperature, the population of polar optical phonons will be greater for the case of ZnO than for GaN.

4.7. A comparison of the bulk results

---

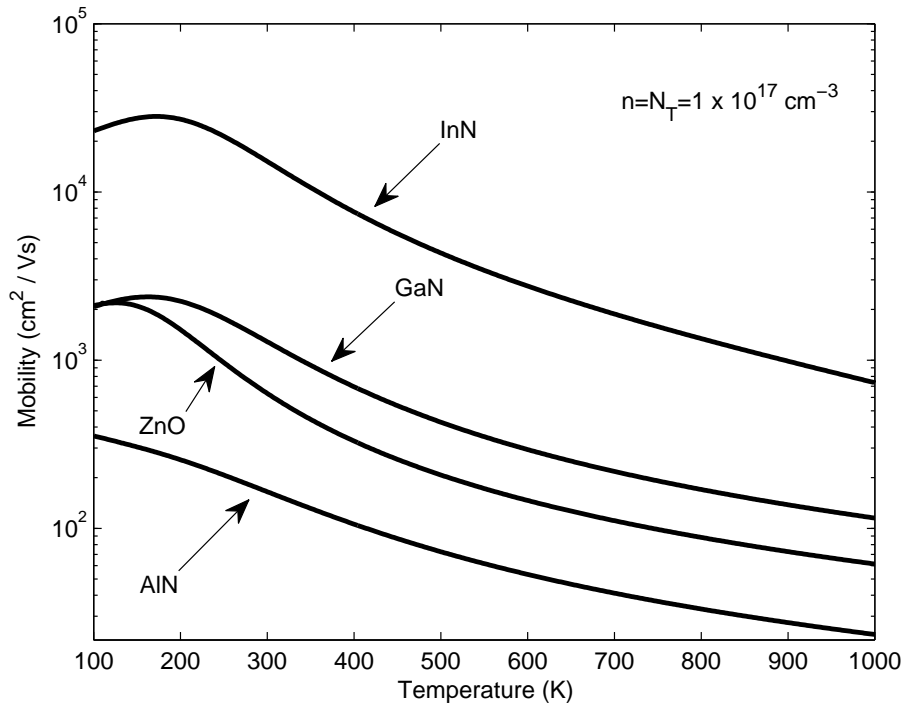


Figure 4.33: The combined low-field electron drift mobility dependence on the crystal temperature for the cases of GaN, AlN, InN, and ZnO. For cases, the bulk ionized impurity is set to  $10^{17} \text{ cm}^{-3}$ . For all cases, the electron concentration,  $n$ , is set to the bulk ionized impurity concentration,  $N_T$ .

As a result, GaN exhibits a higher low-field electron drift mobility; polar optical phonons play a very small role at low temperatures, thus, there is very little difference in the low temperature results for these materials.

## 4.8 Two-dimensional electron gas

At the interface of a wide energy gap/narrow energy gap semiconductor discontinuity, i.e., a heterojunction, a two-dimensional electron gas can accumulate; recall Figure 3.4. The electron concentration within the resultant quantum well can exceed the bulk ionized impurity concentration, electrons from the neighbouring regions pouring into such a well. Thus, in order to study how the low-field electron drift mobility within the two-dimensional electron gas is influenced by the presence of such a well, with the bulk ionized impurity concentration,  $N_T$ , held fixed at  $10^{17} \text{ cm}^{-3}$ , the dependence of the low-field electron drift mobility on the electron concentration,  $n$ , is examined, increases in the electron concentration beyond the bulk ionized impurity concentration being expected. This dependence is determined for GaN, AlN, InN, and ZnO, as is shown in Figures 4.34, 4.35, 4.36, and 4.37. For all cases, the ionized impurity, polar optical phonon, piezoelectric, and acoustic deformation potential scattering mechanisms are considered, Eq. (3.10) being used in order to evaluate the resultant combined low-field electron drift mobility. The observed enhancements in the combined electron drift mobility within the two-dimensional electron gas beyond the bulk results is quite significant in many of the cases. The exact reasons for these functional dependencies lies beyond the scope of this examination.

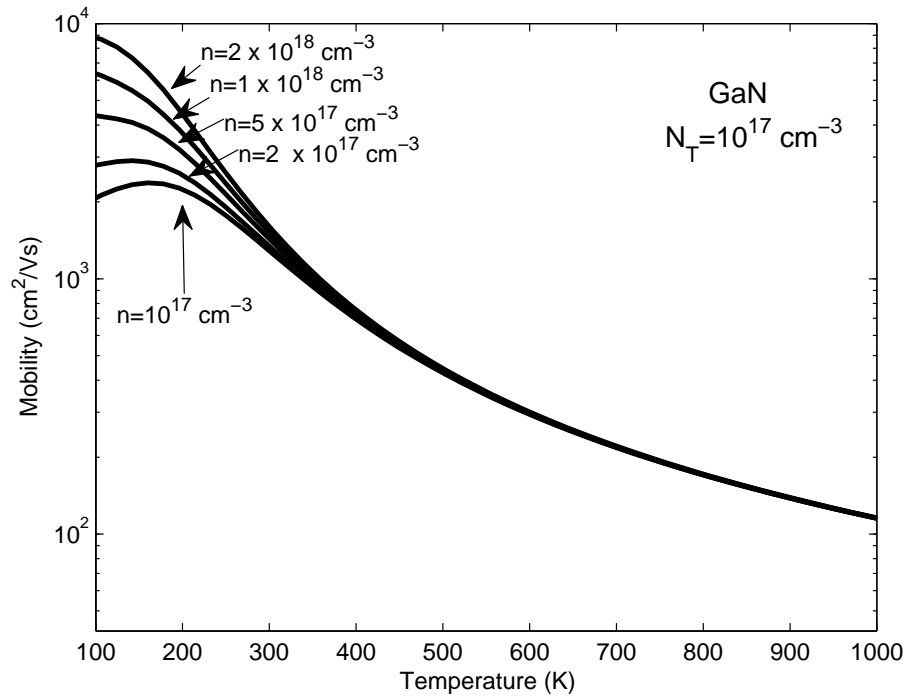


Figure 4.34: The combined low-field electron drift mobility as a function of the crystal temperature for the case of GaN for various electron concentrations. The bulk ionized impurity concentration,  $N_T$ , is set to  $10^{17} \text{ cm}^{-3}$  for all cases.

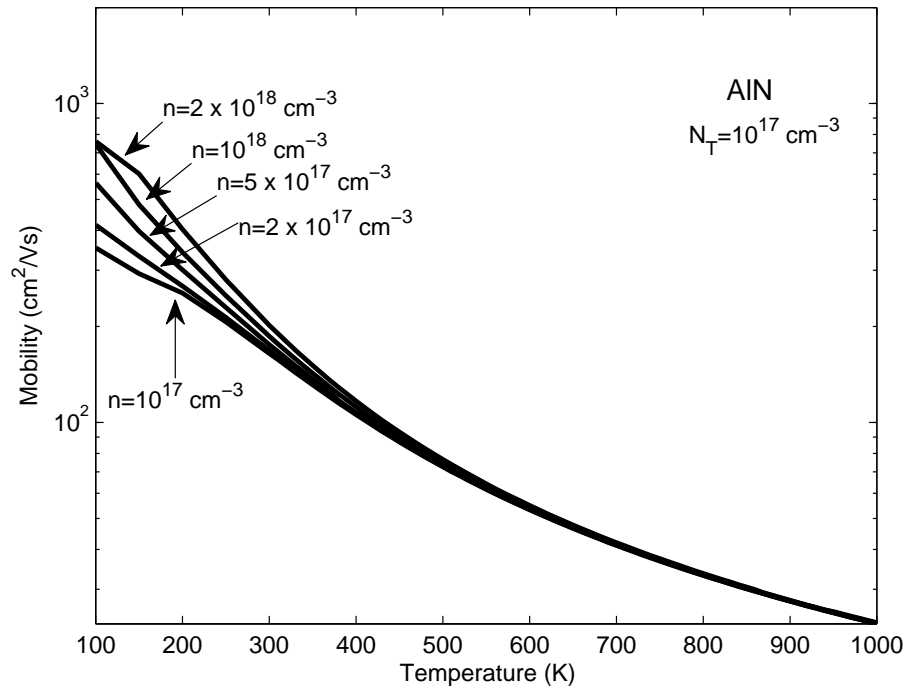


Figure 4.35: The combined low-field electron drift mobility as a function of the crystal temperature for the case of AlN for various electron concentrations. The bulk ionized impurity concentration,  $N_T$ , is set to  $10^{17} \text{ cm}^{-3}$  for all cases.

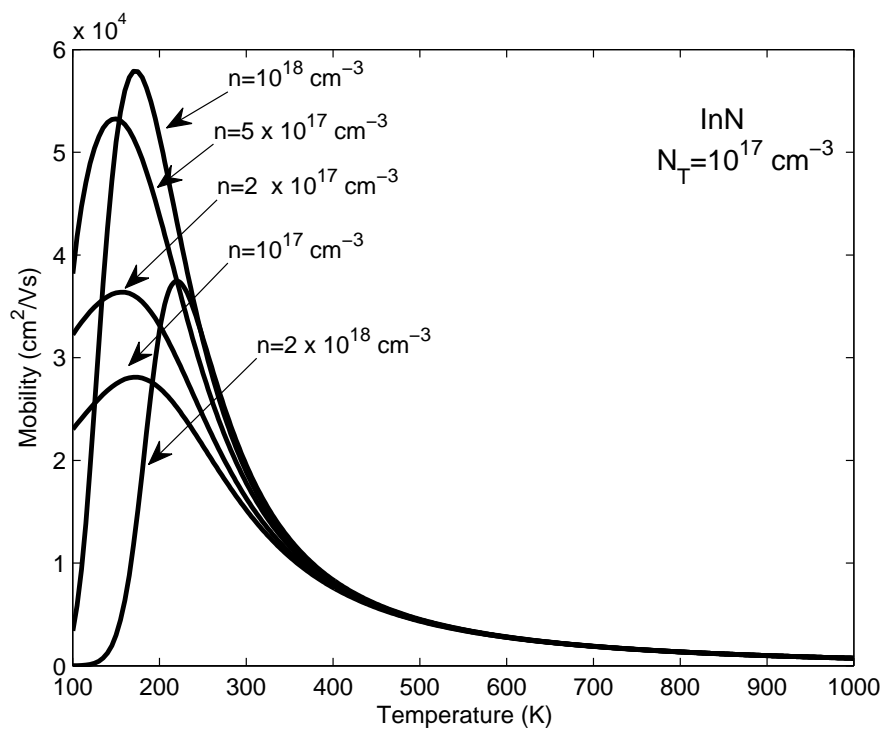


Figure 4.36: The combined low-field electron drift mobility as a function of the crystal temperature for the case of InN for various electron concentrations. The bulk ionized impurity concentration,  $N_T$ , is set to  $10^{17} \text{ cm}^{-3}$  for all cases.

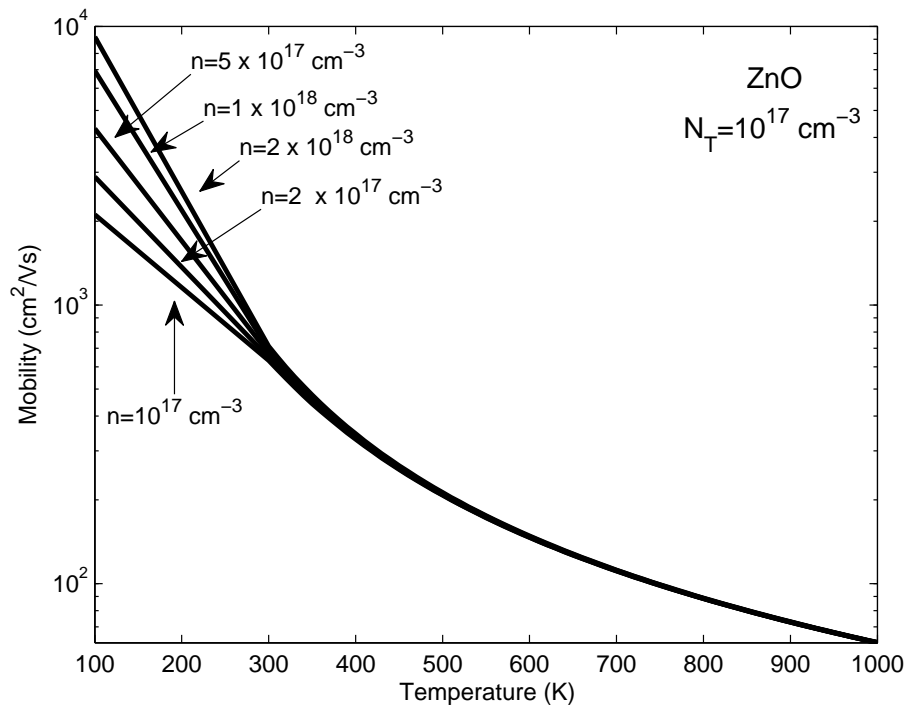


Figure 4.37: The combined low-field electron drift mobility as a function of the crystal temperature for the case of ZnO for various electron concentrations. The bulk ionized impurity concentration,  $N_T$ , is set to  $10^{17} \text{ cm}^{-3}$  for all cases.

## Chapter 5

# Conclusions

In conclusion, the dependence of the low-field electron drift mobility associated with a number of wide energy gap semiconductors on the crystal temperature was determined. The materials considered in this analysis included the wide energy gap semiconductors GaN, AlN, and ZnO. InN was also considered as it is a material that can be alloyed with GaN to produce a wide energy gap semiconductor alloy. The bulk results were determined assuming that the electron concentration,  $n$ , is equal to the bulk ionized impurity concentration,  $N_T$ , for all the cases. It was found that the low-field electron drift mobility associated with InN is greater than those associated with GaN and ZnO, which in turn are greater than that exhibited by AlN. This is due to the light effective mass associated with the electrons in InN and the much heavier effective mass associated with the electrons in AlN; the effective mass of the electrons within GaN and ZnO is between these extreme cases. The two-dimensional electron gas results were obtained by examining the sensitivity of the results to variations in the electron concentration,  $n$ , with the bulk ionized impurity concentration,  $N_T$ , set to a fixed value, the variations in the electron concentration beyond the bulk ionized donor concentration arising as a result electrons from the neighbourhood

of a two-dimensional quantum well leading to an increase in the electron concentration beyond the bulk ionized impurity concentration,  $N_T$ . These electrons within the resultant two-dimensional electron gas will act to screen the ionized impurities, and thus, lead to dramatic enhancements in the low-field electron drift mobility beyond the bulk results.

In this thesis, a number of original contributions have been made. The assembly of material parameters corresponding to the wide energy gap semiconductors GaN, AlN, and ZnO represents a useful contribution to the literature, as does that corresponding to the narrow energy gap semiconductor InN. The dependence of the low-field electron drift mobility on the crystal temperature, something that had heretofore only been done for the case of GaN by Shur *et al.* [18], also represents a useful addition to the literature. The identification of the individual contributions to this mobility, something that had only been done for the case of GaN by Shur *et al.* [18], also represents an original contribution to the literature. Finally, an examination of the low-field electron drift mobility within a two-dimensional electron gas configuration is an novel contribution that points to fertile avenues for further investigation.

There are a number of issues that could be further explored in the near term future. These topics for further investigation include the application of the present low-field electron drift mobility results to electron device modeling, the further development of expressions for the various contributions to the low-field electron drift mobility, and a more proper analysis of the distribution of charge, and its effect on the low-field electron drift mobility, associated with the two-dimensional electron gas that is present at the inter-

face of a wide energy gap/narrow energy gap semiconductor discontinuity, such as that present at the AlGa<sub>N</sub>/Ga<sub>N</sub> interface. Each of these topics is briefly addressed below.

The low-field electron drift mobility results that have been developed within this thesis may be applied for the purposes of electron device modeling. The transport of electrons within an electron device plays an important role in determining the performance of such a device. While high-field electron device applications are beyond the scope of the low-field analysis that has been presented within this thesis, low-field electron device applications abound. The use of the obtained low-field electron drift mobility results to an examination of the potential of each material considered for electron device applications would certainly be a worthwhile pursuit. Comparisons of the performance of various materials and device configurations could greatly benefit the community, and would be relatively easy to implement.

A second important theme that could be explored in the near term future would be a critical comparison between the low-field electron drift mobility results obtained using the analytical expressions of Shur *et al.* [18] and those determined by others, such as the analyses of Nag [19], Sze [14], Chin *et al.* [22, 23], and Walukiewicz *et al.* [24]. A deeper examination of the analyses of Shur *et al.* [18] may allow for an assessment of the physicality of these expressions to the particular semiconductor material that are being examined; in the initial analysis of Shur *et al.* [18], the low-field electron drift mobility associated with Ga<sub>N</sub> was the focus of attention, the applicability of these results to other semiconductor materials being worthy of further investigation.

A final possible topic for investigation, that builds upon these results, is the development of a simultaneous Poisson's and Schrödinger's equation solver that will allow for the determination of the amount of charge within the two-dimensional electron gas at the boundary of a wide energy gap/narrow energy gap semiconductor discontinuity. This would be a fundamental contribution to the field that would be extremely helpful for future electron device design considerations.

# References

- [1] I. M. Ross, “The foundation of the silicon age,” *Physics Today*, vol. 50, pp. 34–39, 1997.
- [2] R. Muller, *Device Electronics for Integrated Circuits*. New York: Wiley, 2003.
- [3] B. Streetman, *Solid state electronic devices*. Upper Saddle River, N.J: Pearson/Prentice Hall, 2006.
- [4] M. A. Green, “Intrinsic concentration, effective densities of states, and effective mass in silicon,” *Journal of Applied Physics*, vol. 67, no. 6, pp. 2944 –2954, mar 1990.
- [5] J. B. Casady and R. W. Johnson, “Status of silicon carbide (SiC) as a wide-bandgap semiconductor for high-temperature applications: A review,” *Solid State Electronics*, vol. 39, no. 96, pp. 1409–1422, 1996.
- [6] U. Hilmi, “A thermodynamic model for determining pressure and temperature effects on the bandgap energies and other properties of some semiconductors,” *Solid State Electronics*, vol. 35, no. 9, pp. 1343 – 1352.
- [7] D. G. Avery, D. W. Goodwin, W. D. Lawson, and T. S. Moss, “Optical

## References

---

- and photo-electrical properties of indium antimonide,” *Proceedings of the Physical Society. Section B*, vol. 67, no. 10, p. 761, 1954.
- [8] S. Adachi, *Properties of group-IV, III-V and II-VI semiconductors*, ser. Wiley series in materials for electronic and optoelectronic applications. John Wiley & Sons, 2005.
- [9] H. P. Maruska and J. J. Tietjen, “The preparation and properties of vapor-deposited single-crystal-line GaN,” *Applied Physics Letters*, vol. 15, no. 10, pp. 327–329, 1969.
- [10] W. M. Yim, E. J. Stofko, P. J. Zanzucchi, J. I. Pankove, M. Ettenberg, and S. L. Gilbert, “Epitaxially grown AlN and its optical band gap,” *Journal of Applied Physics*, vol. 44, pp. 292–296, 2009.
- [11] Özgür, Ya, C. Liu, A. Teke, M. A. Reshchikov, S. Dougan, V. Avrutin, S. J. Cho, and H. Morkoc, “A comprehensive review of ZnO materials and devices,” *Journal of Applied Physics*, vol. 98, no. 4, pp. 041 301+, 2005.
- [12] S. M. Malik, “A density of states and joint density of states analysis of hydrogenated amorphous silicon,” Master’s thesis, University of Regina, 2002.
- [13] Y. P. Varshni, “Temperature dependence of the energy gap in semiconductors,” *Physica*, vol. 34, no. 1, pp. 149–154, 1967.
- [14] S. M. Sze, *Physics of Semiconductor Devices*, 2nd ed. Wiley-Interscience, Nov. 1981.

## References

---

- [15] S. K. O’Leary, B. E. Foutz, M. S. Shur, and L. F. Eastman, “Steady-State and Transient Electron Transport Within the III-V Nitride Semiconductors, GaN, AlN, and InN: A Review,” *Journal of Materials Science: Materials in Electronics*, vol. 17, pp. 87–126, 2006-02-08.
- [16] J. S. Blakemore, “Semiconducting and other major properties of gallium arsenide,” *Journal of Applied Physics*, vol. 53, pp. R123–R181, 2009.
- [17] J. R. Chelikowsky and M. L. Cohen, “Nonlocal pseudopotential calculations for the electronic structure of eleven diamond and zinc-blende semiconductors,” *Phys. Rev. B*, vol. 14, pp. 556–582, Jul 1976.
- [18] M. Shur, B. Gelmont, and M. A. Khan, “Electron mobility in two-dimensional electron gas in AlGaN/GaN heterostructures and in bulk GaN,” *Journal of Electronic Materials*, vol. 25, no. 5, pp. 777–785, 1996.
- [19] B. R. Nag, *Electron transport in compound semiconductors*. Springer-Verlag, Berlin, New York, 1980.
- [20] L. Shen, S. Heikman, B. Moran, R. Coffie, N.-Q. Zhang, D. Buttari, I. P. Smorchkova, S. Keller, S. P. DenBaars, and U. K. Mishr, “Al-GaN/AlN/GaN High-Power Microwave HEMT,” *IEEE Electron Device Letters*, vol. 22, pp. 457–459, 2001.
- [21] J. D. Albrecht, P. P. Ruden, S. Limpijumnong, W. R. L. Lambrecht, and K. F. Brennan, “High field electron transport properties of bulk ZnO,” *Journal of Applied Physics*, vol. 86, no. 12, pp. 6864–6867, 1999.
- [22] V. W. L. Chin, T. L. Tansley, and T. Osotchan, “Electron mobilities in

## References

---

- gallium, indium, and aluminum nitrides,” *Journal of Applied Physics*, vol. 75, no. 11, pp. 7365 –7372, jun 1994.
- [23] V.W.L. and Chin, “The effect of carrier densities and compensation ratios on the electron mobility of  $\text{InAs}_{1-x}\text{P}_x$ ,” *Journal of Physics and Chemistry of Solids*, vol. 53, no. 7, pp. 897 – 904, 1992.
- [24] W. Walukiewicz, H. E. Ruda, J. Lagowski, and H. C. Gatos, “Electron mobility in modulation-doped heterostructures,” *Phys. Rev. B*, vol. 30, pp. 4571–4582, Oct 1984.